RSC Advances

ROYAL SOCIETY OF CHEMISTRY

www.rsc.org/advances

Submitted to *RSC Advances,* May 2015

Advances and Challenges of Sodium Ion Batteries as Post Lithium Ion Batteries

*Monica Sawicki, Leon L. Shaw**

Department of Mechanical, Materials and Aerospace Engineering
Wanger Institute for Sustainable Energy Research,
Illinois Institute of Technology
10 West 32nd Street, Chicago, IL 60616, USA
e-mail: lshaw2@iit.edu

ABSTRACT

Energy and climate concerns have made the need for research towards electrical energy storage. In this context, sodium ion batteries (SIBs) have attracted significant attention lately. Sodium is an abundant resource that is low cost and safe which makes it an attractive alternative to lithium. Its chemical properties are similar to that of Li which makes the transition into using Na chemistry for ion battery systems feasible. This review focuses on the latest progress in both cathode and anode materials for SIBs. It also details research in binders and additives and their effects on the SIB system. It further highlights the optimization of organic electrolytes and ionic liquid based electrolytes for utilization in SIBs. The mechanisms of sodium ion storage, transport, and solid electrolyte interphase formation are also discussed to better understand the behavior of ions and battery materials during de/intercalation. Finally, personal perspectives on outlook and major challenges ahead for SIBs are offered. These comprehensive and in-depth discussions along with proposed directions can enlighten ideas and offer avenues in the rational design of durable and high performance SIBs in the near future.

Keywords: Sodium ion batteries; Anodes; Cathodes; Electrolytes; Binders; Additives.

1. Introduction

Inevitable fossil fuel depletion has made the need for electrical energy storage systems (EES) extremely important. An efficient EES is crucial in order to stabilize the electrical energy grid by supplying a continuous flow of energy during off peak hours of intermittent renewable energy sources (e.g., wind, solar, and wave). The Department of Energy's goal for the cost of energy application on the electric grid to achieve 20% wind penetration is \$100 kWh^{-1} by 2030 [1]. In addition, fossil fuel consumption of internal combustion engines gives rise to environmental pollution and the urgent need for high energy and high power density batteries for hybrid electric vehicles (HEVs), plug-in hybrid electric vehicles (PHEVs) and all electric vehicles (EVs). The battery specification for a 300 mile mid-range electric sedan is an energy density of 250 Wh kg^{-1} at a cost \$125 kWh^{-1} [1–4]. These emerging demands for electrical energy storage can lead to the overall depletion in lithium reserves [2,5,6].

The aforementioned specifications and eventual depletion of lithium have made sodium ion batteries (SIBs) an attractive alternative to lithium ion batteries (LIBs). The advent of the commercialized LIB by Sony in 1991 has made the use of portable electronics a part of everyday life. However, with increased demand for lithium metal arises the concern of the lithium supply because of its low abundance in the earth's crust, as shown in Figure 1 [4,6–8]. Lithium resources are limited to North and South America, China, Australia, Portugal, and Zimbabwe; increased cost of mining and reliance of foreign import make it a necessity to explore alternative battery chemistries. SIBs have gained increased interest since sodium behaves similarly to lithium, is highly abundant, and low in cost as shown in Table 1 [2,4,6]. Furthermore, Na-based anodes allow the use of aluminum as a current collector which doesn't form a binary alloy with sodium, leading to further reduced cost (Table 1).

Although SIBs are a promising alternative, they typically have poor electrochemical activity when compared to LIBs. This is due to two intrinsic shortcomings associated with Na. First, Na has a lower ionization potential than Li, leading to lower operating voltages and thus lower energy densities in comparison to LIBs. Second, Na^+ ions are heavier and larger than Li^+ ions, leading to slow diffusion within a solid electrode during cycling of SIBs and often larger volume expansion of the electrode, as well as lower energy densities when compared with LIBs [2–4,6]. These intrinsic deficiencies give rise to the need for unique crystalline structures with an open framework structure or 3D structures with large insertion channels to facilitate the

intercalation/de-intercalation process of the larger sodium ions [2,3,6,7,9]. In spite of potentially lower gravimetric energy densities than LIBs, SIBs would be an optimal choice for use in EES for renewable sources. The requirements for large scale, stationary storage systems are ultra-long cycle life, high round trip efficiency, low cost, and high safety [2,4,7].

Because of the unique advantages of SIBs over LIBs in the cost and nearly unlimited resources, the interest in SIBs has increased drastically over the last several years. This is reflected in rapid increases in the number of publications on SIBs. Note that there are eight review articles published in 2012-2014 alone [2–4,6,7,9–11]. These reviews have focused on either electrode materials only [7,9,11] or electrode materials plus electrolytes [2–4,9,10]. However, the advancements and challenges in binders, additives and solid electrolyte interface (SEI) layer formation have not been addressed yet. In this review, we will update advancements made in cathodes, anodes and electrolytes while providing critical reviews of the progress made and challenges encountered in binders, additives and SEI layer formation. Furthermore, we will address the scientific understanding of the Na ion transport issue because the analysis of Na ion transport is essential in understanding the overall behavior of SIBs. Finally, we will offer personal perspectives on outlook and major challenges ahead for the target application areas of SIBs. We hope that through these comprehensive and in-depth discussions along with proposed directions can enlighten ideas and offer avenues in the rational design of durable and high performance SIBs in the near future.

2. Sodium Ion Batteries

SIBs were under investigation at the same time as LIBs in the 70s and 80s. LIBs prevailed due to their higher potential and lower mass offering higher energy density; thus shifting the scientific community away from SIB research [4,9,12–21]. As the Li resource demand increases as well as its price, the sodium alternative has been reintroduced into the battery research community. Several chemical structures that do not work for Li intercalation may do so for SIBs which offers research of novel electrode materials [2–4,7,9,22].

The functionality of a SIB is the same as a LIB wherein the electrodes made of intercalating compounds store electrical energy. The battery is made of an anode and a cathode with a porous separator and a conductive electrolyte between them. The potential difference between the two electrodes creates a voltage on the cell. During charging and discharging, sodium ions migrate back and forth between the cathode and anode of the battery based on the

specific redox reaction that occurs between these materials. Figure 2 shows the basic construction and working principle of a SIB [23].

Significant research on SIBs has so far been devoted to organic electrolytes because organic electrolytes can provide higher cell voltages. However, an area of interest to reduce the cost of SIBs is to utilize an aqueous electrolyte for SIBs since it would remove the need for ultra-dry fabrication and thus reduce material and assembly costs. The nonflammability of an aqueous system could provide better safety; and the overall performance may be improved due to high conductivity of aqueous solutions which would, in turn, reduce internal resistance of the battery [4,24–33].

In what follows, we will provide a comprehensive review of cathodes, anodes and electrolytes first, followed by in-depth discussion of the advancements and challenges in binders, additives, Na ion transport, and SEI formation. To assist readers in capturing the breadth and depth of cathode investigations, we have grouped cathodes in five categories according to their chemical compositions. These are oxides, sulfides and sulfates, phosphates, fluorides, and hexacyanoferrates. Similarly, anodes are divided into three groups, including carbonaceous materials, metals and alloys, and metal oxides. Electrolytes are grouped in three categories with organic, aqueous, and ionic liquid-based electrolytes.

3. Cathode Materials

3.1 Metal Oxides

Metal oxide cathode materials are promising candidates for SIBs because there are several processing techniques (e.g., sol-gel method, co-precipitation, solid state reaction, etc.) that can be used to obtain these stoichiometric layered structures. Many of these materials are nanosized which offer large surface area and short diffusion paths for ions during de/sodiation upon cycling. Carbon coating enhances conductivity and offers more homogeneous particle size with uniform structure. For most of the oxide materials, the amount of sodium deintercalated from the cathode material ranges from 0.5 to 0.85. This is dependent on the initial stoichiometry and phase transitions that occur with respect to the change in oxidation states of the metals within the active material. Understanding the electrochemical behavior of the active materials at these different stages will enable the determination of the acceptable Na content range for alkali ion layers.

We will review oxides with a single transition metal component first to emphasize the roles of the crystal structure and redox couples in electrochemical reactions. This will then be followed by reviews of oxides with multiple transition metal components. The use of substitution or doping of other transition metals in the layered oxide structures can offer multiple advantages over oxides with a single transition metal component, including 1) better stability of the material, 2) increased capacity by adding more redox active substitutes, 3) removal of Jahn-Teller distortions, 4) reduction in volume change of the active material, and 5) higher cycling numbers with better capacity retention.

3.1.1 Single Metal Component Oxides

In 1980, Delmas, et al. [15] structurally classified layered oxides of the form A_xMO_2 (A=alkali, M=transition metal) using specialized nomenclature. The layered structure is built by sheets of edge-shared MO_6 octahedra, wherein alkali ions are located between MO_6 sheets. O or P represents octahedral or trigonal prismatic coordination environment of alkali ions, followed by a number describing the number of transition metal layers (3 or 2) in the stacking repeat unit; and O'3 and P'2 represent the monoclinic distortion of O3 and P2 phase packing. The stacking types of O3 and P2 phases are shown in Figure 3 [4]. There are two independent sites for Na in stacked prismatic coordination. One is shared between equal faces above and below the MO_6 octahedra layer (2d), while the second one is shifted by one octahedral group face and shares the edges with the MO_6 octahedra (2b) [2,4,11,15,34].

Sodium intercalation in Na_xCoO_2 bronzes was studied by Delmas et al. [16] in the early 80s. They found that polymorphs of Na_xCoO_2 reversibly intercalated Na^+ over a limited range of $0.5 \leq x \leq 1$ for Na content and the phase transition that occurred was O3 → O'3 → P'3 for the initial O3-$NaCoO_2$ [2,4,16].

Na_xMnO_2 has been widely studied for use as a cathode in NIBs [2–4,7,9,14,29,35–47]. Two phases exist for this material, low temperature α-$NaMnO_2$ is most stable and has an O3 layered structure with monoclinic structural distortion, and high temperature β-$NaMnO_2$ is orthorhombic and contains MnO_2 sheets which consist of edge sharing doubly stacked MnO_6 octahedra. Ma, et al. [36] found that 0.85 Na can be deintercalated from monoclinic $NaMnO_2$ with 0.8 intercalation of Na during cycling giving 185 mAh g^{-1} discharge capacity at a C/10 rate with 71% retention after 20 cycles. Figure 4a and 4b show the voltage profiles for multiple cycles and the voltage profile upon de/intercalation [36].

These voltage profiles show distinct voltage steps and plateaus which indicate different intermediate phase transformations upon de/sodiation. XRD data of pristine $NaMnO_2$ and partially charged $NaMnO_2$ to the midpoint of the 2.63V plateau confirm a two phase transformation from ~$Na_{0.93}MnO_2$ to ~$Na_{0.7}MnO_2$, respectively. The $Na_{0.7}MnO_2$ phase contains six metal layers as opposed to the two layers in $Na_{0.93}MnO_2$ which can be due to Na vacancy ordering or modification of O3 stacking by oxygen layer gliding [36]. Further research must be done in order to determine all phase transformations that occur at the voltage plateaus in the voltage profiles.

Billaud, et al.[47] were able to achieve a high capacity of 190 mAh g^{-1} with β-$NaMnO_2$ at a rate of C/20. This material exhibits good rate capability and capacity retention when cycled at 2C initially offering a discharge capacity of 142 mAh g^{-1} with ~70% (100 mAh g^{-1}) retention after 100 cycles. This compound has a complex structure which contains intergrown regions of α-$NaMnO_2$ and β-$NaMnO_2$ polymorphs.[47] Upon cycling and lowering of the Na content, an increase in stacking faults caused the collapse of the long range order within the material, but was recovered upon Na reinsertion and maintains stable cyclability, even though β-$NaMnO_2$ exhibits increased disorder. This is in contrast to common expectation requiring minimal structural change for reproducible stable cycling.[47]

Jo, et al. [37] investigated the electrochemical behavior of α-$NaMnO_2$ in two different electrolytes, 1M $NaBF_4$ tetraethyleneglycol dimethylether (TEGDME) and 1M $NaClO_4$ ethylene carbonate/diethyl carbonate (EC/DEC). The TEGDME electrolyte has a lower discharge capacity initially (136 mAh g^{-1}) compared to that of the EC/DEC electrolyte but is more stable because after the 20th cycle it retained 74% capacity, whereas EC/DEC only retained 71.6%. The coulombic efficiency maintained over 90% for 1M $NaBF_4$ in TEGDME, while that of 1M $NaClO_4$ in EC/DEC consistently decreased to 80% within 20 cycles. Using EC/DEC offers small bulk and interfacial resistance, but TEGDME has more stable interfacial resistance allowing stable cyclability compared to EC/DEC [37].

Single crystalline sodium manganese oxide ($Na_{0.44}MnO_2$) nanowires are an orthorhombic lattice structure [29]. This structure contains MnO_5 square pyramids and MnO_6 octahedra which form large S shaped tunnels and smaller pentagon tunnels. The S shaped tunnels in $Na_{0.44}MnO_2$ allow mobility of Na ions that can be reversibly extracted and produce a

theoretical discharge capacity of 121 mAh g^{-1}, whereas Na ions are fixed in the pentagonal tunnels and are unable to be extracted. $Na_{0.44}MnO_2$ is a promising cathode material because it has a high capacity of ~120-130 mAh g^{-1} with good cycle performance having 77% retention after 1000 cycles and is capable of being used in non-aqueous and aqueous electrolytes [29,31,35].

Cao, et al. [29] prepared homogeneous and highly crystalline $Na_{0.44}MnO_2$ nanowires and found that they are capable of inserting and extracting four Na ions during cycling inducing a chemical transformation from $Na_6Mn_9O_{18}$ to $Na_2Mn_9O_{18}$. This material delivers reversible capacities of 128 mAh g^{-1} at 0.1C and 82 mAh g^{-1} at 2C. The nanowires are mechanically stable and provide a short diffusion path for de/sodiation. This higher than theoretical capacity result may be due to Na extraction from the pentagonal smaller tunnels [29]. Through density functional theory, XRD measurements, and electrochemical cycling, Kim, et al. [35] were able to confirm this. There are three binding sites for $Na_{0.44}MnO_2$, Na1 corresponds to the almost filled small tunnel, while Na2 and Na3 are half filled in the S shaped tunnels. The Na2 site is broken up into Na21 and Na22 due to different orientation coordination as depicted in Figure 5 [35].

Na21 sites are more stable than Na22 sites since Mn2 and Na2 distance is elongated from repulsive interaction of Na^+ and Mn^{4+} ions. The Na22 sites are only prevalent between $Na_{0.44}MnO_2$ and $Na_{0.55}MnO_2$ due to the competing electrostatic interaction. This forms an unstable biphasic region which induces capacity fading and slow diffusion of Na ions. Seven intermediate phases were identified for sodium insertion and extraction. It was found that the order of extraction started at Na3 sites where sodium ion repulsion is the greatest followed by Na2 and Na1 sites [35]. The results are shown in Figure 6 [35].

Kim, et al. [35] also researched the degree of volume change and evolution of lattice parameters of $Na_{0.44}MnO_2$ during charging and discharging processes. They found that the asymmetric change of lattice parameters is due to Jahn-Teller distortions and calculated that 44% substitution of Cr into $Na_{0.44}MnO_2$ would reduce volume change by 50%.

The intercalation of sodium into layered $NaCrO_2$ has been studied for use in NIBs [17,48–51]. Its rhombohedral (R-3m) O3 type layered structure is similar to that of $LiCrO_2$ but behaves differently since it is electrochemically active with reversible capacities of 120 mAh g^{-1} for the Na ‖ $NaCrO_2$cell (Figure 7a) [48]. $NaCrO_2$ was able to reversibly deintercalate 0.5 mole of

sodium ions per formula unit to form $Na_{0.5}CrO_2$ giving the phase transitions of hexagonal O3 → monoclinic O3 → monoclinic P3 for the charge process. Irreversible Li intercalation of $LiCrO_2$ is due to irreversible migration of Cr(VI) into tetrahedral sites due to disproportionate transfer of Cr(IV) to Cr(III) and Cr(VI). In $NaCrO_2$, Cr(IV) cannot migrate due to the mismatch between $Cr^{VI}O_4^{2-}$ and the O-O bond length and CrO_2 slab distance of the interstitial tetrahedron. Magnetic measurement confirmed that chemically deintercalated $Na_{1-x}CrO_2$ contained Cr(IV) [48,52].

Unfortunately, capacity fading of this material does occur. Ding, et al. [50] used carbon coating on the surface of active $NaCrO_2$ particles to improve electrochemical behavior during cycling. Initial charge and discharge capacities of carbon coated $NaCrO_2$ were 135 mAh g^{-1} and 116 mAh g^{-1}, respectively. The discharge capacity only decreased to 110 mAh g^{-1} after the 40th cycle; whereas naked $NaCrO_2$ had a discharge capacity of ~105 mAh g^{-1} with 0.32% capacity loss for each cycle. The improved performance can be related to the carbon coating since it provides 1) decreased polarization of the electrode, 2) enhanced conductivity, 3) suppression of side reactions between the active material and electrolyte, and 4) slowing of SEI formation at the electrode surface [50].

Overall, $NaCrO_2$ is determined to be a safe electrode material since it is more stable in 1M $NaPF_6$ in EC/DEC than delithiated $Li_{0.5}CoO_2$ and $LiFePO_4$ [51]. The reason for this is due to its high thermal stability. Accelerating rate calorimetry experiments showed lack of heat evolution in $Na_{0.5}CrO_2$. An exothermic reaction did not occur for this material until 250°C with very little release of heat. Thermogravimetric analysis (TGA) showed very small mass change attributing to very little oxygen release. They determined that a reaction between the solvent and $Na_{0.5}CrO_2$ transforms into $NaCrO_2$ and P3-$CrO_{2-\delta}$ which gives minimal oxygen release and accounts for the high thermal stability of this material [51].

$NaFeO_2$ has been considered as a SIB cathode [53–58]. Zhoa, et al. [56] show that it is a thermally stable material with stable reversible capacity of 85 mAh g^{-1} in a Na‖$NaFeO_2$ battery. Differential scanning calorimetry (DSC) measurements showed less heat generation at higher exothermic onset temperatures (220-300°C) offering thermal stability comparable to $LiCoO_2$ counterparts [56]. Recently, hollow iron oxide nanoparticles have been utilized for sodium ion transport. Hollow γ-Fe_2O_3 has cation vacancies which can serve as hosts for Na ions in a voltage range of 1.1-4.0 V. The γ-Fe_2O_3 has been encapsulated between layers of carbon

nanotubes and exhibited a reversible capacity of 189 mAh g^{-1} with 99% coulombic efficiency. An increased C rate of 50 (3000 mA g^{-1}) offered a capacity of 99 mAh g^{-1} with capacity retention for more than 500 cycles [59].

3.1.2 Multiple Metal Component Oxides

Single metal layered structures have offered substantial results that aid in understanding specific phase transitions, thermal behavior of materials, and electrochemical activity. However, multiple metal component oxides provide additional flexibility in increasing the structural stability and energy densities and minimizing the volume change during cycling [35,52,60–67]. Thus, investigation and design of multiple metal component oxides are often built on the success of single metal component oxides.

$Na_{0.45}Ni_{0.22}Co_{0.11}Mn_{0.66}O_2$ can be synthesized using co-precipitation [61] or a solid state reaction [65]. Buchholz et al. [61] found that water treatment rinsing of the co-precipitated material enhances electrochemical performance by stabilizing de/sodiation. The O2 type phase transition along the 4.2 V voltage plateau of $Na_{0.45}Ni_{0.22}Co_{0.11}Mn_{0.66}O_2$ is highly reversible and results in high capacities, high average voltage, and superior cycling performance with a specific capacity of 135 mAh g^{-1} and a coulombic efficiency exceeding 99.7% for more than 250 cycles (Figure 7b) [65].

$Na_{0.45}Ni_{0.22}Co_{0.11}Mn_{0.66}O_2$ was tested in an ionic liquid (IL)-based (10 mol% sodium bis(trifluoromethanesulfonyl)imide (NaTFSI) in N-butyl-N-methylpyrrolidinium bis(fluorosulfonyl)imide ($PYR_{14}FSI$) electrolytic solution and carbonate-based (0.5 M $NaPF_6$ in propylene carbonate) electrolyte [65]. The ionic liquid electrolyte offers higher reversibility for electrochemical de/sodiation due to higher electrochemical stability of the ionic liquid which enables high potential P2-O2 phase transitions at 4.2 V and also hinders solubility of Mn into the electrolyte, offering improved performance at low potentials (2.2 V). A uniform SEI layer formed in batteries tested with the IL-based electrolyte which was beneficial for active material performance, leading to high specific capacities of ~200 mAh g^{-1} and high average voltage (2.7 V vs. Na/Na^+) with capacity retention of about 80% after 100 cycles [65].

$Na_x[Fe_yMn_{1-y}]O_2$ [60,68–70] has gained increased interest as a cathode material because it can obtain the O3 or P2 type structure depending on the sodium/(iron and manganese) ratio. P2 type $Na_{2/3}[Fe_{1/2}Mn_{1/2}]O_2$ delivers 190 mAh g^{-1} (~520 Wh kg^{-1}) of reversible capacity with an

average of 2.75 V vs. Na by utilizing both the Mn^{3+}/Mn^{4+} and Fe^{3+}/Fe^{4+} redox.[60,70] The capacity lowers to ~150 mAh g^{-1} after 30-40 cycles[60,71]. In comparison to lithium, sodium is strongly ionized and has lower covalency with oxygen, thus the iron and oxygen gain more net electtrons. The Fe^{3+}/Fe^{4+} redox is accessible without oxygen loss due to the lower electrochemical potential of the redox reaction, approaching that of Na/Na^{+}.[60,70]

O3 type $Na[Fe_{1/2}Mn_{1/2}]O_2$ is electrochemically active and offers ~110 mAh g^{-1}. This material exhibits a large amount of polarization above 1 V between the oxidation and reduction processes when cycled vs. Na/Na^{+} in the voltage range of 1.5–4.2 V. Although P2 type $Na_x[Fe_yMn_{1-y}]O_2$ is a promising material, some drawbacks exist: (1) large volume change (11.3% shrinkage after charge to 4.2 V) during electrochemical cycles, (2) restriction of sample handling in moist air due to hygroscopic nature (as-preparedP2-$Na_{2/3}[Fe_{1/2}Mn_{1/2}]O_2$ is somewhat oxidized by water, forming P2-$Na_{1/2}[Fe_{1/2}Mn_{1/2}]O_2$ and NaOH), and (3) sodium deficiency in the as-prepared sample.[60,70]

$Na_{0.67}(Mn_{1-x}Mg_x)O_2$ where $x \leq 0.2$ has a P2 type structure has been utilized in a NIB and offers a discharge capacity of 175 mAh g^{-1} (x=0.05).[72] The Mg within the material smooths charge/discharge profiles and cycling stability improves with increased Mg content. This substitution also reduces polarization of the cell [72].

A layered, stable $Na_{2/3}Co_{2/3}Mn_{2/9}Ni_{1/9}O_2$ was prepared by sol gel method which belongs to the $P6_3/mmc$ space group and adopts the P2-type structure [63]. The cathode material delivered a capacity of 110 mAh g-1 when cycled from 2.0 to 4.2 V vs. Na/Na^{+} with coulombic efficiency exceeding 99.4%. The init ial capacity was fully recovered when cycled first at the rate of C/20, then C/10, C/5, C/2, 1C, 2C, and finally C/20 again, demonstrating that this material has good rate capability and cycle stability (Figure 7c) [63]. XRD analysis determined that a transition from the P2 to O2 phase occurred when the concentration of Na reached ~1/3, but this was not confirmed in CV data since this transition would occur at ~4.2 V which was the cutoff voltage for testing. Charge/discharge cycling was then tested between voltages of 2.0-4.5 V, and though the initial capacity increased, there was a large amount of capacity fading as cycling continued which can be attributed to electrolyte decomposition at higher voltage [63].

$Na[Ni_{0.25}Fe_{0.5}Mn_{0.25}]O_2$ (NFM) was placed in a battery with a carbon coated Fe_3O_4 (C-Fe_3O_4) conversion anode and $NaClO_4$ in fluoroethylene carbonate (FEC) and ethyl methanesulfonate (EMS) electrolyte [62]. This group found that 1M $NaClO_4$ in EMS + 2 vol% FEC provided anodic stability of the electrolyte up to 5.6 V vs. Na/Na^+. Moreover, the loading of Fe_3O_4 is higher than carbon since its density (5.17g cm^{-3}) is more than twice that of amorphous carbon (1.8 g cm^{-3}) primarily used as anodes in SIBs. This translates to an increase in energy density of Fe_3O_4 compared to hard carbon. Both NFM and C-Fe_3O_4 electrodes were also separately paired with a Na electrode and charged/discharged at 0.1C. Each electrode showed promising results with 200 mAh g^{-1} for C-Fe_3O_4 and 140 mAh g^{-1} for NFM [62].

Upon charging, the P3 type monoclinic phase is formed and the desodiation proceeds with different transition metals exhibiting different changes in the average oxidation states [62]. Ni^{2+} converts to Ni^{4+} and Fe^{3+} to Fe^{4+} at the end of charge, but almost no change occurs for the oxidation state of Mn. The combined cell of C-Fe_3O_4 | NFM operated at ~2.4 V and delivered a capacity of 130 mAh g^{-1} (Figure 7d) [62]. The structural stability and high electric conductivity of the electrode materials support the rate capability and cycling of this unique battery. The capacity retention was 76.1% at the 150th cycle with coulombic efficiency close to 100% [62].

Yuan, et al. [67] synthesized P2-type $Na_{0.67}Mn_{0.65}Fe_{0.2}Ni_{0.15}O_2$ using a sol-gel method. This stoichiometry improved initial capacity to 208 mAh g^{-1} with 71% capacity retention over 50 cycles. The Ni substitution alleviates Jahn-Teller distortion of Mn(III) and has higher redox reversibility, thereby increasing reversible capacity and stability of the active material [67].

The electrochemical performance of a novel titanium-based O3-type $NaNi_{0.5}Ti_{0.5}O_2$ was explored for the first time as a cathode material. It offers reversible structural change upon de/sodiation [66]. A Na ‖ $NaNi_{0.5}Ti_{0.5}O_2$ cell operated at an average potential of 3.1 V vs. Na/Na^+ and delivered a reversible capacity of 121 mAh g^{-1} at the current density of 20 mA g^{-1} (0.2C). Cycling at an increased rate of 5C delivered more than 60% of the initial discharge capacity, showing that this material has excellent cycle stability and rate capability [66]. Figure 7(e) shows the specific capacity and coulombic efficiency of $NaNi_{0.5}Ti_{0.5}O_2$ as a function of cycle number, exhibiting less than 5% capacity reduction after 100 cycles [66].

3.2 Sulfides/Sulfates

Sodium sulfur batteries exist in molten form (270-350°C) and have been widely used for load leveling and emergency power applications due to their high energy efficiency. The sulfur, sodium, and polysulfide materials are highly corrosive, therefore it is imperative that the seals and containers used for these batteries are resistant and offer protection from water and oxidizing environments. In September 2011 sodium sulfur batteries caught fire at NGK Insulators, Ltd. in Japan. Battery manufacture was suspended until June 2012 after determining the cause of the fire [1,9].

The high temperature and safety issues from use of these batteries have brought attention to the research of room temperature sodium sulfur batteries. Cathodes containing sulfur composites, [73,74] Cu_2S, [75] FeS_2, [76] Ni_3S_2 and Ni_3S_2 with Fe additive, [77,78] $NaFeSO_4F$, [79] and $Na_2Fe_2(SO_4)_3$ [80] are some of the materials studied for use in this type of batteries. The main issues that arise with sulfur containing cathodes are the low utilization of active material, volume expansion upon de/intercalation of Na ions, and polysulfide dissolution into the electrolyte; which are similar to those of Li-S batteries. They also have rapid capacity fading. Researchers have tried to produce Na-S batteries despite these disadvantages due to the high energy density this type of battery is capable of (760 Wh kg^{-1}).

Sulfur composite material consisting of sulfur embedded in a polyacrylonitrile matrix offered thermal stability by retaining above 90% of its original mass confirmed by TGA. This material reversibly reacted with sodium based on the following chemical reaction, $2Na + xS \rightarrow Na_2S_x$. This material delivered a reversible specific capacity of ~500 mAh g^{-1} up to 18 cycles but upon examination of the decrimped battery, dendrite formation occurred which would eventually short the battery [73].

Cu_2S, FeS_2, and Ni_3S_2 with Fe additive offered initial specific capacities of 294 mAh g^{-1}, 447 mAh g^{-1}, and 400 mAh g^{-1} in low voltage potential regions of ~2.0V, respectively [75–77]. These three studies only cycle these batteries for 15, 20, and 50 times. Although they have good coulombic efficiency, capacity fading after the first cycle occurred for these batteries with FeS_2 having the worst electrochemical performance, displaying only ~16% capacity retention. More stable, cyclable sulfide materials need to be studied for the Na-S battery system.

$NaFeSO_4F$ compound has a tunnel type structure and is ionically conductive (7.14×10^{-7} S^3 cm^{-1}) but only ~0.07 Na was extracted from this structure electrochemically involving a 3.6 V Fe^{II}/ Fe^{III} redox plateau. Though extraction was possible, this material offered only ~6% of its theoretical capacity [79].

$Na_2Fe_2(SO_4)_3$ has the most promising results being operable at a voltage of 3.8 V and offering a reversible capacity of over 100 mAh g^{-1} and have 50% capacity retention at a high rate of 20C [80]. The $Na_2Fe_2(SO_4)_3$ is an entirely new material with never reported structure and composition. It is the first sulfate compound with a 3D alluaudite framework and large tunnels along the c-axis (Figure 8a) [80]. Corner sharing bridges together Fe_2O_{10} dimer and SO_4 units. The dimers are formed by Fe ion occupation of edge sharing octahedral sites with crystallographically equivalent octahedron. The sodium ions occupy three specific crystallographic sites, as shown in Figure 8a [80]. The electrochemical data of this material is shown in Figure 8b [80]. This research is the first to obtain the highest known capacity for a Fe-based insertion compound at a high voltage of 3.8 V, making it comparable with Li ion systems. The de/intercalation of all Na sites in this material offers fast Na transport and excellent kinetics providing a battery with cyclic stability (Figure 8b) [80].

3.3 Phosphates

3.3.1 NASICON (Na Super Ionic Conductor)

The NASICON structure ($Na_3M_2(XO_4)_3$ where X = Si^{4+}, P^{5+}, S^{6+}, Mo^{6+}, As^{5+}), especially $Na_3V_2(PO_4)_3$ which is well known for its facile sodium ion conductivity has been studied extensively [81–90]. $Na_3V_2(PO_4)_3$ is a promising candidate for sodium ion batteries because it has a high theoretical energy density of 400 Wh kg^{-1} (117.6 mAh g^{-1} x 3.4V for the V^{4+}/V^{3+} redox couple), and good thermal stability. Figure 9 depicts the NASICON structure studied by Saravanan et al. [81] Corner shared MO_6 and XO_4 polyhedra form a framework with large diffusion channels for sodium ions [81,82].

Saravanan, et al. [81] synthesized $Na_3V_2(PO_4)_3$ nanograins in a conductive network using a novel synthesis method and reached 98.6% of the theoretical capacity of this material. Further, they found that it exhibited high capacity retention at high current rates and also displayed ultra-long life. The intercalation of two sodium ions due to facile sodium ion diffusion in $Na_3V_2(PO_4)_3$ particles accounted for the close to theoretical capacity achievement of the fabricated batteries, offering capabilities that nearly match that of lithium ion batteries.

Figure 10 shows the electrochemical behavior of $Na_3V_2(PO_4)_3$ as a cathode material [81]. Each CV has a high voltage peak at ~3.37 V vs. Na^+/Na and corresponds to the V^{4+}/V^{3+} redox couple. Higher scan rates show a splitting of the cathodic peak at 3.3 V. This may be due to induced local heating at higher scan rates which in turn could lead to structural rearrangement of Na ions from the Na(1) to the Na(2) site. A maximum capacity of 116 mAh g^{-1} was reached at the 0.1C rate. At the 10C rate, 92.2% of the capacity was retained and as the rate increased to 20C and 40C, the retention was 80% and 54%, respectively.

Jung, et al. [88] used a combination of sol-gel method and solid state reaction to synthesize crystalline $Na_3V_2(PO_4)_3$ (NVP) on a graphene sheet surface (NVP/graphene) in order to enhance conductivity. When compared to naked NVP, this composite material exhibited better capacity retention at higher C rates and offers a smaller polarization between charge and discharge curves. The graphene sheets provide a conductive support and offer pathways for ion transport. The stable crystal framework structure of the NVP/graphene composite provides good cyclability and ~96% capacity retention at a 10C rate after 300 cycles [88].

3.3.2 Fluorophosphates

Fluorophosphates have gained increased interest as a new structural host for cathode materials in SIBs. Several studies have been performed on this type of material with different transition metals and compositions using different processing methods [91–98].

Ultrasonic template free spray pyrolysis method was used to form carbon coated hollow 500 nm diameter Na_2FePO_4F spheres with 80 nm wall thickness [91]. Using a low rate of 0.1C, the cathode delivered 89 mAh g^{-1} capacity. At 1C, it offered 75 mAh g^{-1} capacity and provided 80% of this initial capacity after 750 cycles. An increased rate to 9C maintained 33% of capacity. Electrolyte penetration into the nano-sized porous hollow C/Na_2FePO_4F spheres allows the electrochemical reaction to take place on both the outside and inside surfaces of the spheres as well as in the pores. Further, the C/Na_2FePO_4F hollow spheres offer a large reaction area with shortened Na^+ diffusion length. The carbon coating provides structural stability which accommodates volume change during Na^+ insertion/extraction, and electrical conductivity, thus improving charge transfer reaction kinetics and cyclability [91].

Lu, et al. [92] used a solid state reaction to produce $NaVPO_4F$ for use in a SIB. The cell voltage of a battery made of this material mixed with carbon is increased due to the high potential of the V^{3+} to V^{4+} redox transition. The $NaVPO_4F$/C composites (5 wt.% carbon) were tested in the voltage range of 2.5-4.2 V. The $NaVPO_4F$/C composite gave a maximum discharge capacity of 97.8 mAh g^{-1} and had a capacity retention of 81% after 20 cycles. The amount of carbon used for mixing affected the overall performance of the battery, where too much or too little offered low capacity with increased degradation as compared to 5 wt% of carbon used with $NaVPO_4F$. Too much carbon caused large particle size, thereby lengthening the pathway for sodium ion diffusion, making Na de/intercalation from the $NaVPO_4F$ material more difficult [92].

$Na_{1.5}VPO_{4.8}F_{0.7}$ was prepared using a solid state method and generated particles that ranged from 1-5 micron composed of a single crystalline domain [94]. This cathode material is a pseudolayered structure with a space group $P4_2/mnm$. Sodium ion insertion into interstitial sites is provided by the three dimensional open framework of $Na_{1.5}VPO_{4.8}F_{0.7}$ due to corner-sharing between PO_4 tetrahedral and VO_5F/VO_4F_2 octahedral units. The two types of vanadium local environment led to a mixed valence state of vanadium where V^{4+} and V^{3+} ions coexist which offers a tailored vanadium redox couple ($V^{3.8+}/V^{5+}$). The multi-electron redox reaction (1.2 e^- per formula unit) and the high potential (~3.8 V vs Na^+/Na) of the vanadium redox gave an energy density of 600 Wh kg^{-1} with ~95% capacity retention for 100 cycles and ~84% for an extended 500 cycles. This energy density is one of the highest densities ever reported for NIBs [94].

Sodium vanadyl fluorophosphate [$Na(VO)_2(PO_4)_2F$] materials are prepared using solvothermal methods[99–101] capable of extracting 2 Na per unit formula reaching specific capacities of ~100-110 mAh g^{-1} [99,100]. Two voltage plateaus which occur reversibly at 3.6 V and 4.0 V vs Na/Na^+ signify this. Serras, et al.[99] reached the upper limit of this range due to carbon coating of the material which enhanced its electrochemical performance. Impregnation of carbon onto the surface through long thermal treatment resulted in a two phase material consisting of $Na_3(VO)_2(PO_4)_2F$ and $Na_3V_2(PO_4)_3$ which offered an extra plateau at 3.3 V characteristic of the $Na_3V_2(PO_4)_3$ phase. It is well known that it is difficult for $Na_3(VO)_2(PO_4)_2F$ to access its third Na per formula unit, but Xu, et al. [100] have used theoretical calculation to determine how to alleviate this problem. They suggest the

substitution of oxygen with Cl to form $Na_3V_2Cl_2(PO_4)_2F$ which would increase the energy density to 758 Wh kg^{-1}.

3.3.3 Carbonophosphates

Ab initio computational studies have identified transition metal carbonophosphates with the sidorenkite structure, and general formula of $A_3M(CO_3)(PO_4)$ (a=Li or Na, M=Co, Mn, Fe, Ni) as a new class of potential cathode materials [102–104]. This material has an intricate structure with corner sharing of tetrahedral PO_4 groups and MO_6 octhedra forming double layers which accommodate Na atoms at two different interstitial sites. Na(1) sites coordinate with 7 oxygen atoms, and Na(2) sites coordinate with 6 oxygen atoms. The triangular planar CO_3 groups share an oxygen edge with the MO_6 octahedra [104,105]. The decomposition of sidorenkite occurs at ~650°C making solid state synthesis impossible, therefore; a hydrothermal route is used to produce these compounds [103].

Investigation of $Na_3MnCO_3PO_4$ has found that this cathode can exhibit a two electron intercalation reaction upon electrochemical cycling via Mn^{2+}/Mn^{3+} and Mn^{3+}/Mn^{4+} redox reactions with a high theoretical capacity of 191 mAh g^{-1} [105]. However, Chen, et al. [105] were only able to obtain a low specific capacity of 125 mAh g^{-1} experimentally. Recently, Wang, et al. [106] have been able to obtain high specific capacities, reaching 92% of the theoretical capacity of $Na_3MnCO_3PO_4$ when aided by the addition of 60 vol% carbon black (CB), which provides a continuous CB network interacting with almost all $Na_3MnCO_3PO_4$ particles. These findings show that as long as the low electronic conductivity of this material is alleviated, $Na_3MnCO_3PO_4$ has great potential to be a viable cathode material for NIBs [106].

3.3.4 Pyrophosphates

The unique structure of $Na_4Co_3(PO_4)_2P_2O_7$ has four different Na^+ sites located in a 3D ion channel. This material is a promising candidate for SIBs because it has redox potentials in a high potential region between 4.1 V and 4.7 V and delivers 95 mAh g^{-1} reversible capacity with negligible fading even after 100 cycles [107]. It offers low polarization of charge/discharge reactions, small enough to maintain high potential beyond 4.0 V at high rate capabilities of 25C with 84% retention. Even more promising is the fact that this battery may be capable of running at an even higher voltage of ~5.1 V in order to utilize the Co^{3+}/Co^{4+} redox couple for charge compensation of 4 Na^+ extraction from $Na_4Co_3(PO_4)_2P_2O_7$. A suitable electrolyte,

however, would need to be developed for this too occur, but it would produce an efficient battery with compatibility of high rate potential and high rate capability [107].

$Na_7V_4(P_2O_7)_4PO_4$ or VODP was used in a SIB and offered unprecedented cyclic stability and capacity retention for over 1000 cycles [108]. This material only extracted 3.5 and 3.3 Na ions per formula unit obtaining charge and discharge capacities of 81.5 mAh g^{-1} and 77.1 mAh g^{-1}, respectively [108]. Charging/discharging profiles of this material show that only 1 peak exists for discharging and two separate peaks for charging. Quasi open circuit potential confirmed that this behavior is attributed to different kinetics. Further analysis by XRD and DFT calculations proved that a reversible phase transformation of VODP occurs during Na de/intercalation and is the origin of the single valued voltage behavior of this battery. This intermediate phase is governed by the occupation of Na1 and Na2 sites and their relative stability. The structural transformation that occurs is a rotation of each unit of $(VP_2O_7)_4PO_4$ as depicted in Figure 11 [108]. It is suggested that the rotational behavior buffers differences in lattice parameters between initial and final phases of de/intercalated material. This is in turn beneficial for cell kinetics and overall stability of the material.

3.4 Fluorides

Sodium fluoroperovskites of the form $NaMF_3$ (M=Ni, Mn, Fe) were produced using mechanochemical processes and investigated as cathode materials for NIBs [109,110]. Dimov et al. [110] investigated Fe, Cu and Ni metals but found that $NaFeF_3$ is the most electrochemically active due to its chemical stability and iron's high affinity toward fluorine. Gocheva et al. [109] were only able to obtain 61% of the theoretical capacity (197 mAh g^{-1}) of $NaFeF_3$, offering a reversible capacity of 120 mAh g^{-1} with a mean discharge voltage of 2.7 V. Nanosized (10-600 nm) $NaFeF_3$ were produced using a liquid phase synthesis and exhibited discharge capacities in the range of 170-181 mAh g^{-1} when cycled at low rates of 0.01C regardless of the size range [111]. Smaller well dispersed $NaFeF_3$ particles improved rate performance; and upon cycling at 0.1C or greater offered higher discharge capacities when compared to larger agglomerated particles. Kitajou et al. [112] used roll quenching and annealing to obtain highly crystalline $NaFeF_3$. Their first cycle at a rate of 0.076 mA cm^{-2} between 1.5 V and 4.5 V gave 100% efficiency and provided a high initial discharge capacity of 197 mAh g^{-1} [112]. This is due to the reversible Fe^{2+}/Fe^{3+} redox reaction confirmed by XPS. XRD data also confirmed that sodium insertion and extraction is possible due to the flexibility of the corner sharing matrix and the structural strength of the material [112].

3.5 Hexacyanoferrates

Prussian blue ($A[Fe^{III}Fe^{II}(CN)_6]$, $A=Na^+$ or K^+) and its analogues have been investigated as alkali ion hosts for use as a cathode material in a SIB [26,113–117]. This material has a cubic face-centered structure in which two different metal centers Fe^{3+} and Fe^{2+} are bridged by CN^- groups which provides large ionic channels along the <100> direction enabling facile insertion and extraction of alkali ions [26,114,115,118]. Wessels, et al. [26] were able to insert/extract sodium from nickel hexacyanoferrate in aqueous electrolyte, obtaining a capacity of ~60 mAh g^{-1} at a C/6 rate. An 8.3C rate showed no significant capacity loss after 5000 cycles giving a capacity of ~52 mAh g^{-1} [26]. The retention of this material is promising, but the aqueous system requires low voltage which makes it only suitable for large scale EES.

Yue, et al. [118] synthesized mesoporous crystalline nickel hexacyanoferrate (NiHCF) using synergistically coupled nanocrystal formation and an aggregation mechanism. Different reaction times offer modification of surface morphology, porosity, and crystallinity. This group found that regardless of these characteristics a capacity of ~65 mAh g^{-1} was achieved at low current rates with stable cycling. Using the longest reaction time gave macroporous NiHFC with a smaller surface area and offered the best rate performance, suggesting that larger pores within the structure facilitates more effective Na^+ mass transport [118].

Sodium manganese hexacyanoferrate $NaMnFe(CN)_6$ was synthesized to form two different structures based on sodium content, $Na_{1.72}MnFe(CN)_6$(NMHFC-1, rhombohedral) and $Na_{1.40}MnFe(CN)_6$(NMHFC-2, cubic) [114]. This study compared these two products and found that the sodium ion content of precipitous aqueous solution during synthesis affects composition and structure of the final product. More Na^+ concentration induces higher Na content and a transition from cubic to rhombohedral symmetry. This phase transition is reversible upon cycling; a fully discharged NMHFC-2 sample matches Raman spectra of pristine NMHFC-1 powder. NMHFC-1 has a high reversible capacity of 134 mAh g^{-1} and retains 120 mAh g^{-1} after 30 cycles due to Fe^{III}/Fe^{II} and Mn^{III}/Mn^{II} redox couples. Cycling of NMHFC-1 produces a potential shift where the final redox potential is higher for the Fe^{III}/Fe^{II}, but lower for the Mn^{III}/Mn^{II} couples. The power density and high rate capability of NMHFC-1 make it a promising cathode material [114].

4. Anode Materials

Unfortunately, sodium does not intercalate with graphite which is the most commonly used anode for Li based batteries. Several types of carbons have been investigated such as petroleum cokes [119–121], carbon microspheres [122], carbon black [123], fibres [124], and N-doped carbon nanofibers [125,126]. Stevens and Dahn [127] were able to insert sodium into hard carbon and since then, this material has been investigated extensively by several groups. In addition to carbonaceous materials, pure metals, metal alloys and oxides have been investigated in order to increase the specific capacity and cycle life of the anode. Pure metals and their alloys are attractive due to their high theoretical capacities but often suffer from the problem of pulverization. Oxides have only been investigated for the last 2 to 3 years, but have demonstrated cycle stability up to 450 cycles. Progresses made in these areas are detailed below.

4.1 Carbonaceous

4.1.1 Hard Carbon

Komaba, et al. [128] tested graphite and hard carbon to investigate Na insertion properties with aprotic electrolyte solutions. Graphite was not a suitable anode for sodium ion batteries, and thus hard carbon was tested in a full cell configuration. Testing was done in a beaker type electrochemical cell where hard carbon and $NaNi_{0.5}Mn_{0.5}O_2$ were the working electrodes and a sodium foil was the quasi reference electrode. The hard carbon electrode was first tested in an $NaClO_4$ EC:DMC electrolyte and had an initial capacity of 220 mAh g^{-1} but reduced as galvanostatic cycling continued [128].

Sugar pyrolysis was used to prepare hard carbon (HC) with highest reversible capacity ever reported in the literature (300 mAh g^{-1} at a rate of C/10 after 120 cycles) [129]. This study focused on the effect of ball milling hard carbon as well as electrode processing atmosphere (air or Ar). The use of air or Ar for electrode slurry seemed to have no overall effect on the performance of the battery, suggesting that there is no significant impact on electrolyte decomposition and SEI formation, but also that the surface chemistry of the material is not modified either.

The as-synthesized and ball milled carbon were evealuated in additive free $NaClO_4$ in EC:PC electrolytes. Though the ball milled hard carbon (PBMHC) had higher specific surface area and smaller particles, the as-synthesized hard carbon was more stable and gave a lower

amount of heat generation based on DSC investigation. Therefore, it was beneficial with respect to safety as well. The evaluation of the degree of graphitization based on the integrated intensity of D/G (D=defect-induced D band, and G=crystalline graphite G band ratio of carbon) was found to be the determining feature that gave the difference in reversible specific capacities for these materials (2.6 and 2.1) for hard carbon and PBMHC, respectively) [129].

Hard carbon C1600 was used as an anode in a sodium ion battery and its electrochemical and thermal properties were tested in four different electrolytes: (i) 1 mol dm^{-3} $NaClO_4$/EC:DMC, (ii) 1 mol dm^{-3} $NaClO_4$/PC, (iii) 1 mol dm^{-3} $NaPF_6$/EC:DMC, and (iv) 1 mol dm^{-3} $NaPF_6$/PC [130]. The C1600 performed best with 1 mol dm^{-3} $NaClO_4$/EC:DMC giving an initial capacity of 413 mAh g^{-1} with retention of 90% over 50 cycles [130]. Based on TGA/DSC testing done in a temperature range from RT to 400°C, C1600 anodes were more thermally stable in EC:DMC based electrolytes. The onset temperatures of exothermic heat for sodiated C1600 in 1 mol dm^{-3} $NaClO_4$/EC:DMC were lower than that of the lithiated electrode in the same electrolyte. This proves that this mixture of anode and electrolyte for Na batteries is more stable than that for Li ion batteries in spite of the instability of Na metal compared to Li [130].

Hard carbon is an advantageous material to be used as an anode, but other carbonaceous materials have been studied as well. These materials are nanosized sheets [131], wires [132], or N-doped fibers [125,126] with structural stability and interconnected networks which offer accommodation of volume expansion and good conducting connectivity.

4.1.2 Carbon Nanostructures

Peat moss (PM) was used as a precursor to form a three dimensional macroporous interconnected network of carbon nanosheets with 60 nm thickness [131]. Highly cross linked lignin and hemicellulose rich structure of the peat moss suppresses graphite formation and instead forms highly ordered pseudographitic arrays with 0.388 nm intergraphene spacing. The PM macroporous network has micro and mesopores which shortens the diffusion length of the Na^+ ion and also offers electrolyte penetration on all sides of the material and enables Na^+ intercalation to occur at low voltage (0.2 V vs Na/Na^+). These pores buffered sodiation induced expansion/contraction in the matrix during cycling. The use of this material as an anode gave low voltage/low hysteresis plateau behavior and resembled capacity vs. potential

profiles of graphite anodes in LIBs. It also provided a stable cycling capacity of 298mAh g^{-1} with nearly 100% coulombic efficiency with 85% capacity retention at the 210th cycle [131].

Pyrolyzation of a hollow polyaniline nanowire precursor was performed to prepare hollow carbon nanowires (HCNWs) [132]. Cycling this material at a 0.2C rate between 0.01-1.2 V delivered a high reversible capacity of 251 mAh g^{-1} with 82.2% capacity retention over 400 charge−discharge cycles [132]. Na insertion into the carbon was obtained due to the size and structure of the HCNWs which offered short diffusion distances for Na ions, but the interlayer spacing (0.37 nm) between graphitic sheets also enabled good Na-insertion. Theoretical calculations revealed that a minimum spacing of 0.37 nm is needed for Na ion intercalation since the energy barrier for Na ion insertion (0.053 eV) is low enough to conquer. Na ions undergo two types of insertion−extraction mechanisms for this material. The voltage range of 0.2−1.0 V produced a reaction characterized by a charge transfer mechanism on the surface of the small graphitic clusters. The lower voltage range of 0.0−0.2 V mechanism was related to Na ion insertion−extraction in the graphitic interlayers [132].

Introduction of a hetero atom into a carbonaceous anode material was proven beneficial for enhancing electrochemical performance in LIBs. This approach was used for SIBs where polypyrrole precursors were pyrolized in an inert atmosphere to obtain N-doped interconnected carbon nanofibers [125,126]. N-doping generates extrinsic defects which can enhance reactivity and electronic conductivity of the carbon. O-containing and N-containing functional groups exist on the surface of the nanofibers. The redox reaction between functional groups and active sites on the surface of the carbon layer attribute to Na ion adsorption and desorption and electron transfer. Cycling of this material showed that a pseduocapacitance can be generated due to the interaction between the electrolyte and N species on the surface. An increased amount of pyridinic and quaternary nitrogen gives better electrochemical performance and higher pseudocapacitance. Overall the interconnected N-doped nanofibers offered large interlayer distance and enhanced Na ion transport which gave high rate capability and stable cyclability. The only drawback is the low average voltage of ~1 V vs. Na/Na^+, but these materials may still be considered due to their rate performance [125,126].

4.2 Metals/Alloys

Pure metals or metal alloys are attractive due to their high theoretical capacities but their main drawback is pulverization. The larger ionic radius of Na makes the effect of volume expansion upon de/sodiation more detrimental in causing irreversible structural changes to the anode. Continued cycling often compromises the structure of the Na host and leads to rapid cycle fading [133–138]. Some metals (Sn and Sb) form binary alloys with sodium and have been known to aggregate and alloy into larger particles isolating in the electrode and further disrupting the integrity of the material. Sn or Sb based anodes[133,135–137] with specific structural properties are introduced which aid in the reduction of aggregation, and also buffer volume expansion upon cycling with sodium.

The mechanical behavior of crystalline Na-M (Sn, Pb, Si, and Ge) alloys were investigated by Mortazavi, et al. [138] using first principles simulations to determine their intrinsic elastic properties during sodium intercalation. The elastic moduli of pure M phases changed by 75% from sodiation. The elastic moduli decreased linearly with Na concentration. This elastic softening originated from a transition to weaker interatomic bonding. Na-Si and Na-Ge have low values for the B_H/G_H ratio which indicates low resistance toward brittle failures; therefore, these alloys would be susceptible to fracture upon sodiation. The electronic charge distribution analysis for each system reveals that upon sodiation M-M bonds are replaced with ionic Na-M bonds [138].

The structural stability of the material upon sodiation is at risk, but it is important to understand the behavior of these alloys in order to fabricate Na-ion electrode architecture that can improve the mechanical stability of these materials. The functional relationship between Na^+ concentration and elastic moduli can be used to determine deformation and fracture of these materials using simple continuum models [138]. Some unique metal or metal alloys produced by using novel techniques to fabricate a material that was capable of handling volume expansion and improving cyclic stability are reviewed below.

High energy ball milling of red phosphorus powder with Super P carbon black at a ratio of 7:3 for 24 hours produced an amorphous nanocomposite sample with highly dispersed phosphorous clusters in a carbon matrix [134]. This structure can buffer the 490% volumetric expansion of phosphorus to Na_3P upon conversion-type reaction with 3 Na atoms. The fully charged Na_3P form Na_2P, NaP, and NaP_7 intermediates during charge/discharge cycling. The

initial discharge capacity was 1750 mAh g^{-1} with stable reversible capacity during the first 40 cycles. The capacity gradually dropped to ~1200 mAh g^{-1} but with 99% coulombic efficiency [134]. Increased current density to 4000 mA g^{-1} resulted in charge capacity loss at the low voltage plateau of 0.2 V. Electrochemical impedance spectra revealed that the charge transfer resistance of sodium ion insertion was ten times higher than that of the extraction process for this material. When fully charged using a current density of 250 mA g^{-1}, the material is easily discharged at several rates and can maintain about 95% of its potential capacity [134].

Unique nanorods with a core shell structure composed of C/Sn/Ni were synthesized to form a 3D nanoforest binder free composite electrode [133]. Vertical alignment of the rods with interdigital spacing accommodated volume expansion/contraction of the alloy during sodiation/desodiation. The carbon coating on the Sn layer of the nanorods improved electrochemical performance by providing conductivity and suppressing aggregation and pulverization of Sn during cycling. Figure 12 demonstrates this unique structure and its electrochemical behavior [133]. The electrochemical performance of this anode material was investigated in coin cells using Na metal as the counter electrode, and 1M $NaClO_4$ in ethylene carbonate/diethyl carbonate (EC:DEC, 1:1 by vol %) as electrolyte. Sn anodes provided around 730 mAh g^{-1} at the first desodiation process and retained 55% initial capacity after 150 cycles [133].

Sn thin film deposition on a carbon nanotube coated hierarchical wood fiber substrate was utilized as an anode in SIBs, giving an initial discharge capacity of 339 mAh g^{-1} with ~43% retention after 400 cycles [137]. The ductility of the wood substrate (circumferential stiffness 0.7-3.0 GPa) enabled sodiation by releasing mechanical stress during cycling. The anodes were analyzed after 400 cycles in the fully charged state and a wrinkled structure on the wood fibers was observed. This surface change was correlated to fiber deformation and attributed to the improved cycling performance of the battery by reducing rupture of the SEI layer and minimizing exposure of the Sn to the electrolyte, thereby keeping the morphology of the Sn surface intact and preventing pulverization [137].

The mesoporous structure of the fibers acted as an electrolyte reservoir, offering ion transport among all surfaces of the fibers and improving the kinetics of Na ion transport. Figure 13a and 13b illustrate ion transport pathways and electrochemical activity with respect to blocked and unblocked pathways [137]. The lightweight substrate of the wood fibers offered excellent

mechanical properties, large surface area, and a porous structure which improved cycling stability and provided effective ion and electron transport [137].

Sn nanoparticles were mixed with Poly(9,9-dioctylfluorene-co-fluorenone-co-methylbenzoic ester) (PFM) conductive binder (Sn/PFM) and used in a sodium ion battery delivering 806 mAh g^{-1} and 610 mAh g^{-1} at C/50 and C/10 rates, respectively [135]. PFM binder caused isolation of Sn nanoparticles, but due to its conductivity all nanoparticles were electrically conducting and able to reversibly cycle close to the theoretical capacity. The study only had 10 cycles for testing of each type of electrode. Initial results of the first ten cycles do correlate well to the suggested behaviors of the electrodes, but more cycling needs to be done in order to determine if the Sn/PFM is highly reversible with coulombic efficiency at several C rates over a long period of time [135].

Electrospinning was used to create an antimony/carbon electrode with Sb nanoparticles of ~30 nm which were uniformly encapsulated in interconnecting 1D 400 nm carbon fibers (SbNP@C). The Sb/carbon ratio was estimated to be 54 to 46 (in weight) based on TGA results. The electrode was completely binder free, and did not require a carbon additive for conductivity. This material was able to endure over 300 cycles under a current density of 100 mA g^{-1}, maintaining an overall discharge capacity of 350 mAh g^{-1} [136]. The electrodes were able to handle high current density cycling and delivered total reversible capacities of 273, 185, 123, and 88 mAh g^{-1} at the current densities of 1.0, 2.0, 4.0, and 6.0 A g^{-1}, respectively [136]. Upon disassembly, SEM images showed that the SbNP@C electrode maintained its structural integrity and flexibility thereby withstanding expansion due to sodiation. The SbNP@C microstructure was also effective in stabilizing the SEI film. The Sb nanoparticles did undergo a transformation to even smaller amorphous particles, but remained within the carbon fiber core, thus confirming the mechanical stability of the fiber.

Based on the results of these experiments for metal and alloy anodes, the use of specialized structures of nanosize whether chemically synthesized or fabricated from a naturally sourced substrate are effective in accommodating volume expansion to buffer the stress in the anode from the de/sodiation process. Some of the results obtained are the first of their kind with respect to rate capability and is a marked improvement from previous studies. Further research needs to be done in order to cycle these materials at higher C rates with longer life.

4.3 Metal Oxides

Xiong, et al. [139] were one of the first groups to utilize an all oxide Na ion battery using TiO_2 nanotubes as an anode and a $Na_{1.0}Li_{0.2}Ni_{0.25}Mn_{0.75}O_{\delta}$ as a cathode. The cell had an operating voltage of 1.8 V and a discharge capacity of ~80 mAh g^{-1} [139]. This group found that the diameter of the nanotube (> 80 nm ID) is critical for Na intercalation. Solvated Na ions are too large to infiltrate smaller diameter nanotube pores, and this size imbalance limits the capacity of the structure. TiO_2 has been further studied in the form of nanocrystals [140], and microspheres [141] as anodes in SIBs which have been able to successfully intercalate sodium ions.

Anatase TiO_2 nanocrystals were used as anodes in a sodium ion battery. They exhibited a stable reversible charge capacity of ~150 mAh g^{-1} and could withstand high rate cycling of 2 A g^{-1} without degradation [140]. The tetragonal crystal structure of anatase TiO_2 offers pathways for Na diffusion as it is made up of 3D networks of stacked 1D zig zag chains which consist of distorted edge sharing TiO_6 octahedra. This group tested the as synthesized material (ANC), but also prepared a TiO_2/carbon composite (ANC-C) for battery testing and comparison. Each sample had particle sizes in the 10-15 nm size range with similar particulate morphology. The ANC-C sample gave lower capacity than ANC, but it was more efficient with less charge transfer resistance. The added carbon to the ANC-C nanoparticles offers conductivity, and a higher specific surface area enables a lot more diffusion of ions during cycling.

Carbon coated TiO_2 microspheres [141] were utilized as an anode in a SIB. The microspheres were primarily TiO_2 crystallites whose growth was suppressed from carbon coating during calcination. The uniform carbon coating enhanced electrical conductivity while preventing agglomeration of the crystallites and thus shortening the diffusion paths for Na^+ ions. The electrochemical properties were evaluated as a function of carbon content, and the TiO_2-6.8 wt % C electrode exhibited the best cycle performance (100% cycle retention during the 50th cycle) and the best rate capability, delivering the discharge capacities of 155 mAh g^{-1} at 0.1 C, 149 mAh g^{-1} at 1 C, and 82.7 mAh g^{-1} at a 10 C rate, respectively [141].

$Na_2Ti_3O_7$ has been researched as a promising intercalation compound. Two dimensional sheets of $Ti_3O_7^{2-}$ which share edges with triple octahedral chains accomodate Na ion transport [6,142–145]. Rudola, et al. [143] acheived 177 mA g^{-1} at a C/10 rate with relatively stable capacity

retention [143]. Zhang, et al. [145] synthesized a three dimensional spiderweb architecture of $Na_2Ti_3O_7$ nanotubes which offers charge capacity of 425 mAh g^{-1} (0.05 rate), and can deliver 107 mAh g^{-1} (0.5C rate) after 500 cycles with capacity loss of only 28% with coulombic efficiency of ~100%. The use of P2 type layered $Na_{2/3}Co_{1/3}Ti_{2/3}O_2$ provides ~90 mAh g^{-1} (0.2C rate) of reversible capacity with ultrastable cyclability with 84.84% capacity retention for 3000 cycles (5C rate), and structural stability (0.046% unit cell volume decrease) even after 500 cycles of sodium de/intercalation [146]. A potential anode for grid scale applications whose structure facilitates sodium intercalation is $Na_2Ti_6O_{13}$. It offers a capacity of 20 mAh g^{-1} (20C rate) that is capable of cyclability of 5000 times with ~75% capacity retention [147]. TGA analysis also showed thermal stability with little weight loss until 500°C making it a safe material for prolonged use in a grid system.

A copper oxide (CuO) nanowire array (CNA) was prepared using in-situ engraving of Cu foil to produce a binder and additive free anode for use in a SIB (Figure 14a) [148]. The aligned, porous, arrayed structure of the CNAs offered ample space for volume expansion during cycling which reduced pulverization. Further, this porous structure facilitated electrolyte diffusion and electron transport. The contact between the CNAs and the Cu current collector provided a framework for the electrochemical reaction to begin at the Cu substrate and spread to the whole electrode. This helped to retain morphological integrity of the CNAs. The in-situ formed interconnected metallic Cu particles served as electron transporting paths between the Cu substrate and the unreacted CuO close to the tips of the CNAs.

Figure 14a and 14b show the schematic of the CuO arrays and the electrochemical behavior of binder free CNAs at a high current density of 200 mA g^{-1}, respectively [148]. A high initial discharge capacity of 640 mAh g^{-1} (close to the theoretical capacity of 674 mAh g^{-1}) was obtained using a high current density of 200 mA g^{-1} which corresponds to 1.9 sodium ions per formula unit. XRD results indicated that reduction reactions during discharge were attributed to the conversion of CuO into intermediate phases ($Cu^{II}_{1-x}Cu^{I}_{x}O_{1-x/2}$, Cu_2O) and the decomposition of Cu_2O into Cu and Na_2O.[148] The anode exhibited good cycle stability up to 450 cycles. However, irreversible capacity loss did occur on the initial charge which could hinder practical application, but conductive coating or doping of the CNAs may alleviate this problem. Further research in this area must be employed [148].

5. Electrolytes

Interfacial reactions between the electrolyte and electrode surfaces are a key factor in understanding SEI layer formation and charge transfer kinetics during cycling of sodium ion batteries. The investigation of different electrolytes for use in SIBs is essential in order to determine the optimal electrolyte composition for enhanced electrochemical performance of battery materials. The electrolytes studied so far can be broadly grouped into three categories: organic electrolytes, aqueous electrolytes, and ionic liquid based electrolytes. The progress made in these systems is summarized below.

5.1 Organic Electrolytes

Jang, et al. [149] have investigated sodium perchlorate ($NaClO_4$) salt mixed with binary solvents as electrolytes for SIBs. The electrolytes were 1M $NaClO_4$ dissolved in a solvent mixture of ethylene carbonate (EC)/diethylene carbonate (DEC) (1/1, v/v) (EC/DEC/1M $NaClO_4$), or ethylene carbonate (EC)/propylene carbonate (PC) (1/1, v/v) (EC/PC/1M $NaClO_4$). Galvanostatic cycling of a SIB with a $Na_4Fe_3(PO_4)_2(P_2O_7)$ cathode was done between 1.7 and 4.2 V at a rate of C/20 for pre-cycling and C/10 for cycling [149]. It is found that the PC based electrolyte which has a higher dielectric constant than DEC showed higher ionic conductivities with $NaClO_4$ concentrations greater than 0.5 M and was stable at potentials up to 4.7 V vs. Na/Na^+, whereas the DEC based electrolyte began oxidizing at 3.6 V on the stainless steel electrode used for this testing parameter. The decomposition of DEC forms organic radical species ($CH_2CH_2\cdot$) which then react with EC. The decomposition products accelerate decomposition of the electrolyte and diffuse to the cathode, creating a thick film. XPS measurements also confirmed that ClO_4^- anion decomposition was accelerated by these decomposition products. The EC/PC/1M $NaClO_4$ electrolyte offered more stable electrochemical performance of the $Na_4Fe_3(PO_4)_2(P_2O_7)$ making it a better candidate for use in this SIB [149].

Ponrouche, et al. [150,151] studied several different organic based electrolytes to determine the optimal electrolyte for a cell with hard carbon vs Na anode. All tested electrolytes consisted of a 1M salt: sodium bis(tri-fluoromethanesulfonyl)imide, sodium perchlorate, or sodium hexafluorophosphate (NaTFSI, $NaClO_4$, or $NaPF_6$, respectively) in: propylene carbonate (PC), ethylene carbonate (EC), diethyl carbonate (DEC), dimethyl carbonate (DMC), dimethoxyethane (DME), tetrahydrafuran (THF), or triethylene glycol dimethyl ether (Triglyme). The three salts were also tested in 50/50 wt% mixtures of EC:DMC, EC:DME,

EC:PC, and EC:Triglyme. The group tested the viscosity, ionic conductivity, and stability (electrochemical and thermal) as well as their electrochemical performance.

It is found that there is improved ionic conductivity of mixed solvents with lower viscosity values than single solvent based electrolytes. In addition, the ionic conductivity is found to be proportional to the dielectric constant of the EC co-solvent except for PC and Triglyme which decrease ionic conductivity due to their increased viscosity. The use of a co-solvent therefore improves dissociation of a salt and enhances ionic conductivity [150]. The thermal stability of the single solvents, binary solvents and salts were tested using DSC experiments. The $NaClO_4$ was found to be the most stable followed by $NaPF_6$ and NaTFSI. The trend for thermal stability of single solvents is PC>EC>DEC>DMC>DME. EC:PC was found to be the most thermally stable binary solvent. The electrochemical potential windows of each salt in PC as well as $NaClO_4$ in all of the different single solvents and binary solvents are tested, and the results are shown in Figure 15 [150].

The EC:PC with $NaPF_6$ was the optimal electrolyte to be used as a standard electrolyte in NIBs with hard carbon as the anode. Although the $NaClO_4$ based electrolyte offered more stable cyclability giving a reversible capacity of ~200 mAh g^{-1} with decent rate capability and over 180 cycles of capacity retention, the $NaPF_6$ based electrolyte showed better SEI thermal stability with the highest exothermic onset temperature of 156.2°C for full sodiation of hard carbon [150].

This group went even further in their studies in a following report based on electrolyte optimization through the addition of a third low viscosity co-solvent [152]. The viscosity and conductivity were analyzed using an EC:PC mixture with 1M $NaClO_4$, $NaPF_6$, or NaTFSI and the addition of a co-solvent with a fixed composition of $EC_{0.4}$:$PC_{0.4}$:$U_{0.2}$, U being either DEC, DMC, or DME. The introduction of these following co-solvents decreased viscosity and enhanced ionic conductivity following the trend: DME > DMC > DEC [152].

NaTFSI salt was used in this study [152] in order to determine cation-anion interaction based on salt solvation since the $TFSI^-$ anion is considered the best probe for solvation. The solvation shell of sodium cations is mainly composed of EC with very little contribution from the other solvents or anion. This showed that there is no significant modification to the solvation shell

by DMC addition, and that increased ionic conductivity was due to the decrease in the viscosity of the electrolyte.

DMC content influence was further studied using EC:PC:DMC electrolyte with the NaTFSI salt using a difference of content from 0-50 wt% for DMC while the EC:PC ratio was maintained at 1:1. Based on the Arrhenius plot as shown in Figure 16 [152], it was found that the most thermally stable composition with respect to DMC content was $EC_{0.45}$:$PC_{0.45}$:$DMC_{0.1}$. The ionic conductivity of the electrolyte with the small addition of DMC was improved over the whole range of temperatures used, making $EC_{0.45}$:$PC_{0.45}$:$DMC_{0.1}$ the best electrolyte choice for use in testing HC and $Na_3V_2(PO_4)_2F_3$ vs. Na/Na^+ as well as in a full HC ‖ $Na_3V_2(PO_4)_2F_3$ cell.

Full Na-ion cells had an operation voltage of 3.65 V, very low polarization, and excellent capacity retention upon cycling with reversible capacity of ~97 mAh g^{-1} for more than 120 cycles with high coulombic efficiency (>98.5%) [152]. Figure 17a and 17b show the voltage vs. capacity profiles of the full cell at different C rates and the insets show charge capacity and efficiency, as well as a schematic of the full cell [152].

These studies [150–152] have been very informative with respect to organic based electrolytes. This information is beneficial to the SIB community because there are not many other studies that are so in depth with respect to all of the different organic solvents and Na salts. Utilizing this information to accommodate the voltage potentials of active materials in a battery can offer optimized performance by choosing an optimal electrolyte.

5.2 Aqueous Electrolytes

Among various studies of aqueous batteries [24–28,30,31], Na_2SO_4 in deionized water is a popular electrolyte, but other Na based salts such as NaCl and $NaNO_3$ can also be used. Kim et al. [31] found that the use of an aqueous electrolyte with $Na_{0.44}MnO_2$ gave better rate capability and kinetic behavior as opposed to non-aqueous electrolytes. This was due to the difference in the apparent diffusion coefficient (1.08×10^{-13} to 9.15×10^{-12} cm^2 s^{-1} in aqueous system and in the range of 5.75×10^{-16} to 2.14×10^{-14} cm^2 s^{-1} in non-aqueous systems) [31].

$Na_3V_2(PO_4)_3$ (NVP) in a three-electrode system was tested between 0 and 0.9 V vs standard calomel electrode (SCE) in 1M Na_2SO_4 [30]. Several factors such as 1) unwanted oxidation of

H_2O, 2) electrode material dissolution in aqueous electrolyte, and 3) structure variation of active material during de/intercalation have been identified that can cause performance decay of aqueous SIBs, leading to low capacity retention (~32% at 30th cycle) and unsatisfactory coulombic efficiency of ~80% [30].

A full aqueous SIB was built using $Na_2V_6O_{16}\cdot nH_2O$ as anode and $Na0.44MnO_2$ as cathode by Deng et al. [27] They found that the diffusion of sodium ions was provided by pathways formed in the interstices between V_3O_8 layers where hydrated sodium ions are located. An irreversible structural change occurs upon sodium intercalation which caused rapid capacity fade of the battery [27].

A promising aqeous battery system to date is composed of a $Na_{0.44}MnO_2$ cathode witha a $NaTi_2(PO_4)_3$ anode with 1M Na_2FesO_4 electrolyte. This battery maintains ultrafast rate performance (>100 C) with cycling stability surpassing 1500 cycles.[33] This cell delivers ~120 mAh g^{-1} of reversible capacity. XRD results show each electrode retains structural stability even during high rate cycling. The battery is most stable at C > 1. The capacity fade at low rates could possibly be related to partial dissolution of the electrodes, and oxidation of the anode or electrolyte.[33]

The use of an aqueous SIB would be very advantageous because of the huge abundance of Na resources, reduced cost, and safety; but there are drawbacks. The structural stability needs to increase in order to tolerate de/intercalation and stabilize capacity. Complications that arise with the use of aqueous batteries are 1) elimination of residual O_2 in the electrolyte, 2) inhibition of H_3O^+ co-intercalation into the electrode, and 3) efficient internal consumption of O_2 and H_2 produced from cathode and anode sides when overcharged or overdischarged or improperly operated in a closed aqueous battery system. These all need to be addressed and overcome for the practical application of an aqueous battery system [4].

5.3 Ionic Liquid Based Electrolytes

Ionic liquids (IL) are attractive as solvents for electrolytes because they have low flammability, negligible vapor pressure, a wide electrochemical/chemical/thermal stability and high ionic conductivity [153,154]. The use of NaTFSI in N-butyl-*N*- methylpyrrolidinium bis (trifluoromethanesulfonyl) imide ($PYR_{14}TFSI$) was studied as an ionic liquid electrolyte based on conductivity and stability using different concentrations of NaTFSI [154] and utilized

in a Na ‖ $Na_{0.45}Ni_{0.22}Co_{0.11}Mn_{0.66}O_2$ cell [65]. Monti et al. [153] used the same salt but instead used 1-ethyl-3-methylimidazolium bis(trifluoromethylsulfonyl)imide (EMImTFSI) and 1-butyl-3-methylimidazolium TFSI (BMIm-TFSI) as solvents.

Ionic conductivity of the ionic liquids decreased with an increased amount of NaTFSI, as evidenced in Figures 18a and 18b for different IL solvents [153,154]. This behavior is similar to Li based ILs, but Na based ILs had slightly higher conductivity. The increase of Na^+ ions from NaTFSI replacing ionic liquid cations caused increased interaction of high charge surface density Na^+ ions with $TFSI^-$. The ions try to counterbalance each other and in turn increase viscous drag, and reduce ionic transport, thus lowering ionic mobility and conductivity. The IL electrolytes show no sign of crystallization or phase transitions at room temperature which can be attributed to the different sizes of the Na^+ and IL cations. The amorphous phases over a wide thermal window produced conductivities greater than 1 mS cm^{-1}, values close to that of Li based IL electrolytes. This in turn makes the IL based electrolytes a safe, and viable candidate for room temperature SIB batteries [153,154].

Chagas, et al. [65] found that the use 10 mol% NaTFSI in $PYR_{14}TFSI$ provided higher reversibility of the de/sodiation process due to the increased electrochemical stability of the ionic liquid. The higher voltage (> 4.2 V) P2-O2 phase transition of $Na_{0.45}Ni_{0.22}Co_{0.11}Mn_{0.66}O_2$ in the Na ‖ $Na_{0.45}Ni_{0.22}Co_{0.11}Mn_{0.66}O_2$ cell was able to occur because of the larger electrochemical potential voltage window. Another advantage of using IL based electrolytes is that the dissolution of Mn in the $Na_{0.45}Ni_{0.22}Co_{0.11}Mn_{0.66}O_2$ cathode material did not occur at low voltages. The battery had high cycling stability and much higher discharge capacity compared to the same type of cell cycled in a PC based electrolyte.

The use of a proper electrolyte with specific active materials can improve the overall SIB system by enhancing ionic mobility and improving cyclability and retention. Ionic liquid based electrolytes with low salt concentration were optimal for ionic conductivity and overall performance of a tested SIB. IL based electrolytes do have an increased potential window which can be utilized for transition metal redox reactions that occur above the 4.0 V plateau. Plus, the use of this type of electrolyte makes it safe due to low flammability and volatility. Another safe electrolyte for use in the SIB is aqueous based, but low operating voltages may not be suitable for their practical application. The rapid capacity fading of the SIBs with aqueous electrolyte also needs to be improved before they can compete with SIBs which use

organic or IL based electrolytes. Ponrouche, et al. [150,152] found that mixtures of organic solvents gave higher conductivity and enhanced the overall performance of SIBs. These investigations [27,30,150,152–154] reveal that the study of specific additives or materials for use in a SIB is critical in order to understand how they affect the overall performance of SIBs.

6. Binders/Additives

There is not much research with respect to electrolyte additives for SIBs. Komaba, et al. [23] recently tested several well-known Li ion battery additives in a SIB system and found that fluoroethylene carbonate (FEC) was efficient in improving the reversibility of sodium insertion in a Na aprotic cell with a hard carbon anode and $NaNi_{0.5}Mn_{0.5}O_2$ based cathode. The addition of FEC improved capacity retention by suppressing decomposition of the propylene carbonate electrolyte solvent. FEC initially decomposed adding a voltage peak at 0.7 V during the first reduction. It is believed that this initial decomposition is critical in modifying the surface passivation layer, thereby increasing the electrochemical performance of the cell. In this same study, *trans*-difluoroethylene carbonate (DFEC), ethylene sulfate (ES), and vinyline carbonate (VC) were also tested as potential additives. It was found that DFEC had no beneficial effects, ES addition had a detrimental effect toward Na cells, and VC decreased reversible capacity of the cells [23].

In another study by Komaba, et al. [128], VC was added to PC in a 49:1 volume ratio for beaker-type cells with hard carbon or $NaNi_{0.5}Mn_{0.5}O_2$ as the working electrode and sodium foil as the quasi reference. Results show that it had a negative effect on Na insertion into the hard carbon anode. These findings led to the testing of the material in a coin type cell with the PC electrolyte and no additives. The initial efficiency of this cell reached 90%, which is believed to be due to the different cell configuration giving a more uniform current distribution [128].

A recent study by Dahbi, et al. [155] found that the use of carboxymethyl cellulose binder (CMC) is superior when compared to commonly used PVDF for hard carbon negative electrodes in NIBs; and that the effectiveness of FEC was dependent upon its combination with such binders. A CR2032 coin cell was tested between 0 and 2.0 V vs. Na^+/Na where Na metal was the counter electrode and the anode consisted of hard carbon in a 90:10 ratio with CMC or PVDF. Based on their results, anodes with CMC without the use of the FEC additive in a 1M $NaPF_6$ PC electrolyte gave better cyclability by preventing electrolyte decomposition, and providing a preformed SEI layer on the hard carbon electrode. FEC with PVDF binder

has a synergetic role in surface morphology and electrochemical behavior of hard carbon electrodes. FEC aided in forming a passivation layer on the hard carbon electrodes with PVDF and was necessary to improve cycle performance [155].

Some studies pertaining to LIBs have found that the use of poly(vinylidene fluoride) (PVDF) is detrimental to the battery. Traditionally, this material is used to integrate electroactive particles; however, it has been found to accelerate the deterioration of cycling stability and cause irreversible capacity losses [148,156,157]. The addition of this electrochemically inactive and insulating material impedes the performance of the active material because it can swell during cycling and reduce structural stability; thereby reducing cycle performance. The addition of these materials also leads to increased manufacturing costs which is of importance for EES. These findings are for LIBs but since the SIBs are similar in many ways, it is important to take these findings into consideration.

More studies related to binder addition and electrolyte additives are needed in order to determine optimal conditions for use of such materials in SIBs. A binder or additive that may be detrimental for LIBs has been found to be better for SIBs and vice versa, so it is imperative for the research community to understand how certain materials can inhibit or enhance the performance of SIBs.

7. Sodium Ion Transport

The insertion and removal of sodium was compared to those of lithium by Komaba, et al. [128] in order to discuss the mechanism. Li insertion tends to occur between graphene layers and in hard carbon nanopores around the sloping and plateau regions of potentiograms between 0 and 1.2 V, and the sodium curve has a flat plateau at ~ 0.1 V, as seen in Figure 19 [128].

Sodium insertion into hard carbon was analyzed using XRD to determine the structural change that occurs around this voltage. A pristine electrode was first analyzed and then compared to a hard carbon electrode reduced at 0.2 V. The Bragg peak at 23.4° for the pristine electrode shifted to a lower angle at this reduced voltage, indicating that the spacing between graphene sheets expanded to accommodate sodium insertion in between the parallel layers. Upon oxidation to 2.0 V, the peak returned to its original position in the pristine condition, indicating the reversibility of the sodium. Small angle X-ray scattering (SAXS) and Raman spectroscopy data further confirm the structural change of the hard carbon due to

reversible sodiation. For SAXS, the nanopores in hard carbon were assigned a scattering intensity of 0.03 to 0.07 Å when the electrode was electrochemically reduced from 0.2V to 0V [128]. The intensity decreased reversibly attributing to reversible sodium ion insertion into the nanopores since the electron density contrast between the nanopores and carbon matrix decreased. Raman data showed that a shift occurred which signifies the elongation of the C-C bond (G-band) upon insertion during the low voltage sloping region, and upon approaching a voltage of zero, this G-band stays put, indicating there was no change in the state of the negatively charged graphene layers. The Na behaved as Li does with respect to Raman data when it is lithiated, but NMR and XPS studies need to be done in order to confirm if the Na forms quasimetallic nanoclusters in the nanopores of hard carbon, as Li does [128].

Gotoh, et al. [158] used solid state ^{23}Na NMR to investigate sodium insertion into a hard carbon electrode of a SIB to confirm that quasi-metallic cluster formation does not occur. The state of sodium in the hard carbon was studied in comparison to Li intercalated carbon. Carbon was mixed in a 90:10 weight ratio with PVDF to form the cathode and Na metal was used as the counter electrode in a coin type cell. 1M $NaClO_4$ in PC:FEC (98:2 volume ratio) was used as the electrolyte. Galvanostatic testing at 0.5 mA cm^{-2} in a range of 2-0 V vs Na/Na$^+$ was used to cycle the batteries. Each battery was removed at a different charge level and studied with NMR. Samples with higher state of charge showed peaks at 5.2 and 9.9 ppm which correlate to reversible sodium stored between disordered graphene sheets in hard carbon. Peaks at -9 to -16 ppm were assigned to sodium in heterogeneously distributed closed nanopores in hard carbon. Though these results show sodium insertion during charging, the speed at which Na$^+$ ions diffuse between different sites of hard carbon is slow in NMR time scale since it doesn't form quasi-metallic clusters in closed nanopores like Li at low temperatures [158].

Deng, et al. [27] studied the diffusion behavior of Na ions in $Na_2V_6O_{16}\cdot nH_2O$ and found that there was a linear relation between the CV peak current and the square root of the scan rate which indicated solid-state diffusion of Na ions in the host material during de/sodiation. Based on this, the diffusion coefficient of Na in $Na_2V_6O_{16}\cdot nH_2O$ in an aqueous battery was estimated using the Randles–Sevcik equation [27]

$$i_p = 0.4463\left(\frac{F^3}{RT}\right)^{1/2} n^{3/2} A D^{1/2} C * v^{1/2} \quad (1)$$

where i_p is the peak current, F is the Faraday's constant, R is the gas constant, T is the absolute temperature, n is the number of exchanged electrons, v is the scan rate of CV, C is the concentration of sodium ion, A is the actual surface area of the electrode, and D is the diffusion coefficient of sodium ion. The calculated diffusion coefficient of sodium ion (D_{Na}) in the $Na_2V_6O_{16}\cdot nH_2O$ nanobelts was $2.46x10^{-14}$ cm^2 s^{-1} [27]. The 1D nanostructure was able to overcome the detrimental effect of the low D_{Na}, but capacity fading was quick for the battery. The low performance of the battery was attributed to an irreversible structure change of $Na_2V_6O_{16}\cdot nH_2O$ that occurred during cycling.

Overall, the fundamentals of sodium ion transport have not attracted sufficient attention of the scientific community although this is an important area for charge/discharge kinetics and in some cases is critical for the cycle stability. The transport of Na ions during cycling is a pivotal parameter with respect to reversibility and retention. The cathode or anode material needs to have pathways to enable short, fast diffusion of Na ions during de/sodiation. Many groups have focused on creating unique structures for ion mobility with hope of obtaining optimal diffusion during cycling. They have been successful, but understanding exactly how ions diffuse in a specific structure, and the diffusion coefficient of the ion could aid in determining how to enhance or change a structure in the future to further improve the kinetics and cycle stability. Also, studying how the diffusion coefficient changes in the presence of different electrolytes would be beneficial in understanding how the salt and solvent affects diffusion of ions during cycling, but this type of study has not yet been undertaken.

8. SEI Layer Formation

The formation of the solid electrolyte interphase is a very critical aspect with respect to the performance of SIBs. The SEI layer forms in the first charge/discharge cycle due to electrolyte decomposition and is primarily the reason for initial capacity loss in the first cycle. This passivation layer then further protects the electrode by inhibiting side reactions of the electrolyte with the interfacial surface upon continued cycling. Since SEI layers consist of electrolyte decomposition products that are insoluble, the composition of the electrolyte has a strong impact on their properties such as ionic conduction, stability, and thickness [150]. The SEI layer has many criteria, it should: 1) be electronically insulating to inhibit further reduction of the electrolyte, 2) reduce the reduction and oxidation kinetics to improve the electrolyte stability, and 3) allow transport of cations to be intercalated during cycling

[128,150,152]. The thermodynamic stability of organic solvents at ~0 V vs. Na^+/Na is not stable; therefore, passivation plays a key role in cycle performance of sodium insertion [128].

Komaba, et al. [128] carried out a comparative investigation for passivating surfaces for hard-carbons in Na and Li cells. The morphology of hard carbons cycled in Li and Na cells was observed using SEM and confirmed sub-micrometer sized particles dispersed on the electrode surface. Na cells had larger unevenly distributed particles as compared to Li cells which had a uniform deposit layer. TEM analysis showed that the layers, whether uniform or not, were ~30 nm in dry conditions.

X-ray photoelectron spectroscopy (XPS) measurements revealed the difference of the surface layers formed by the electrochemical cycling. The XPS spectra have a strong peak at 284.5 eV which is assigned to the sp^2 carbon in C-C of graphene in hard carbon, while other peaks originate from the PVDF binder [128]. The strongest peak almost disappears after cycling, indicating that the hard carbon in both cells was covered with the decomposition products of the electrolyte. Figure 20 shows the XPS data [128].

The XPS data shows that the $-CH_2-$ peak intensity is stronger for the Li cell and corresponds to a larger amount of hydrocarbon compounds in its surface film. Another interesting characteristic is that the sp^2 carbon became more clear and intense in the C 1s spectra which indicated that the surface layer in the Na cell is actually thinner than that in the Li cell [128]. The further investigation of this passivation layer using time-of-flight secondary ion mass spectroscopy (TOF-SIMS) showed that the surface film in the Na cell was composed of inorganic compounds, whereas the passivation layer for Li cells was composed of organic compounds, as previously stated. Figure 21 shows the TOF-SIMS results [128].

These results show that the SEI layer allows for the reversible Na insertion of hard carbon. The SEI morphology and chemical composition differed for the Na and Li cases even though the same electrode and electrolyte material were used. The only difference was the intercalant alkali element. Further research is ongoing to determine the formation process and conductivity of the SEI layer for Na cells [128].

Ponrouche et al. [129] also investigated the SEI layer formation and found the same behavior for XPS results and confirmed that the SEI thickness is about the same as the XPS analysis depth

(~5-10 nm). The carbonaceous species that composed the SEI layer were very similar to those observed by Komaba, et al [152].

9. Outlook and Major Challenges Ahead

Significant and rapid progress of SIBs has been made in the last 5 years, as evidenced by the fact that 80% of the publications reviewed in this article are published in the last 5 years. The speedy advancement in SIBs can be attributed to the similarity between LIBs and SIBs in their operating principles [22] which greatly shortens the learning curve and expedites the progress of SIBs. In fact, the progress made in SIBs is so large that the properties of SIBs can now compete with that of LIBs in some application areas. Tables 2 and 3 summarize the specific capacities and numbers of cycles that have been achieved experimentally for the most promising cathodes and anodes of the SIBs investigated so far, respectively. Based on these experimentally accomplished values, the potentials of SIBs in competing against LIBs in three critical application arenas, portable electronic devices, electrical grid and electric vehicles, can be offered below.

Portable electronic devices such as cell phones, laptop computers, iPod and MP3 player are currently powered by LIBs capable of at least 200-300 cycles with retentioin of 80% of their capacity [159]. $LiCoO_2$ with a specific capacity of 155 mAh g^{-1} is most widely used as the cathode in commercial LIBs and, when coupled with the graphite anode (350 mAh g^{-1}), provides a cell voltage of 3.8 V and a specific energy of 408 Wh kg^{-1} (based on the electrode materials only) [160]. Such a specific energy and the required cycle life (200 cycles or more) are gradually approached by SIBs. For example, one may pair a $Na_{1.5}VPO_{4.8}F_{0.7}$ cathode [94] with a carbon nanostructure anode[131] to make a SIB with a 210-cycle life and a specific energy of 299 Wh kg^{-1} at the beginning of the battery life and 284 Wh kg^{-1} at the end of 210-cycle life, based on the data listed in Table 2 and the cell voltage of 3.3 V (with the $Na_{1.5}VPO_{4.8}F_{0.7}$ cathode at the average potential of 3.8 V vs Na/Na^+ and the carbon nanostructure anode at the average potential of 0.5 V vs Na/Na^+) [94,131]. $Na_xFe_yMn_{1-y}O_2$ would also be a great material to compete with LIBS due to its estimated energy density of 520 Wh kg^{-1} based on an average operating voltage of 2.75 vs. Na/Na^+, [60,71] but needs to be able to cycle longer in order to replace the LIB in the future with respect to the required cycle life. With the additional improvements of SIB electrodes in the near future and the significant cost advantage of SIBs over LIBs based on the raw material prices and the use of Al current collectors (Table 1), it is

safe to conclude that SIBs will be strong contenders with LIBs in the areas of portable electronic devices and power tools in the next several years.

In the area of grid-scale electrical energy storage for renewable energy integration, frequency regulation, peak shaving and voltage regulation, the volumetric and gravimetric energy densities of batteries are not critical. In contrast, ultra long cycle life (> 20,000 cycles and calendar life of 15 to 20 years), high round trip efficiency (> 90%), low cost and sufficient power capability are the major requirements. In light of these requirements, SIBs would be advantageous over LIBs because Na is highly abundant, low cost, and environmentally friendly. In this context, the porous $Na_3V_2(PO_4)_3$/C cathode [81] has already been demonstrated to be capable of 30,000 cycles (Table 2). The Prussian blue analogue $Na_2MnFe(CN)_6$ has been tested 1,200 cycles and projected to be capable of 10,000 cycles with 95% capacity retention [161]. Therefore, there exist good SIB cathode materials for ultra long cycle life. The progress made in SIB anodes with ultra long cycle life is also very impressive with 3,000 and 5,000 cycles being demonstrated using $Na_{2/3}Co_{1/3}Ti_{2/3}O_2$ and $Na_2Ti_6O_{13}$, respectively [146,147] (Table 3). Nevertheless, continued resarch in increasing the cycle life of SIB anodes and cathodes would be an important research topic in the near future to make SIBs a viable technology for grid-scale energy storage. Saravanan, et al. [81] have predicted that the commercial lead acid batteries currently used in the electric grid would become obsolete if a suitable anode with a stable capacity of ~120 mAh g^{-1} is developed and paired with the $Na_3V_2(PO_4)_3$/C cathode since its energy density would be 10 times greater.

In the area of electric vehicles, the high volumetric and gravimetric densities of batteries are critical. Good cycle life (> 1,000 cycles) is also essential. As mentioned before, based on Na atomic weight and ionic diameter, the energy densities of SIBs will always be lower than that of LIBs. In spite of these constraints, significant progress has been made with cathodes reaching the specific capacity of 145 mAh g^{-1} after 1,200 cycles and anodes reaching the specific capacity of 400 mAh g^{-1} after 150 cycles (Tables 2 and 3). However, further improvements in the energy density are needed and the breakthrough will likely be from developing electrodes with higher operating voltages or electrodes with more than one Na ion insertion or reaction per formula unit. The drawback of the former approach is that the redox reactions that occur at higher voltages than the potential window offered by current electrolytes can be detrimental to the cycle stability of batteries. To harvest the high voltage benefit of this type of electrodes, electrolytes that can withstand high voltages need to be

developed. IL-based electrolytes can offer the potential window that is needed for high voltage electrodes, but such electrolytes are relatively new and need to be tested further. In addition, the cost of IL-based electrolytes needs to be reduced drastically for broad market penetration.

Developing electrodes with more than one Na ion insertion or reaction per formula unit could hold great promise in increasing the energy density of SIBs. The issues associated alloy- and compound formation-type electrodes (e.g., Sn, Si, Sb and P) are often low cycle stability due to significant volume changes during charge/discharge. For example, P has a high capacity but with 491% volume expansion when forming Na_3P during sodiation [162,163]. Such large volume expansion and shrinkage during cycling result in particle pulverization, loss of electrical contact, and unstable SEI. The key to solving this problem is to confine the volume change within a sub-micrometer shell via "core-shell" structures. Such a strategy has been successfully devised to develop the double-walled Si nanotube anode capable of 6,000 cycles for LIBs [164]. The superior cycle stability of the double-walled Si nanotube anode is due to the hollow tube structure which has an inner Si tube covered by an outer SiO_x shell. The inner hollow Si tube has a free surface to allow silicon to expand inward during lithiation and shrink back to its original position during delithiation, whereas the outer SiO_x shell prevents silicon from expanding outwards during lithiation and permits the formation of a stable SEI on its surface [164]. Similar strategies can be utilized for high capacity electrodes with large volume changes for SIBs.

Some efforts have been made in developing electrodes with more than one Na ion insertion per formula unit. These materials such as $Na_3V_2(PO_4)_3$ [81,86–88], $Na_{1.5}VPO_{4.8}F_{0.7}$ [94], $Na_3MnCO_3PO_4$ [106], $Na_4Co_3(PO_4)_2P_2O_7$ [107], $Na_2MnFe(CN)_6$ [114,161], and $Na_2Ti_3O_7$ [142] do exhibit relatively high specific capacities, and in some cases higher than 150 mAh g^{-1} [106,142]. However, further improvements are needed since few offer specific capacities higher than 200 mAh g^{-1} with long cycle life. Future experimental efforts guided by first principles calculations [22,102,165] are expected to accelerate research in this direction to develop electrodes with high specific capacities and superior cycle stability.

10. Conclusion

The abundance and low cost of sodium has made it a promising alternative to lithium for an ion battery system. Research has shown that there are many Na chemistries that are suitable

for SIBs. Some Na based materials with similar structure to that of Li analogues have been found to be electrochemically active where the latter have not, which makes the research of Na based electrodes an exciting endeavor. The larger atomic weight and ionic radius of Na compared to Li generates the need for specialized structures that can facilitate strain and offer short diffusion paths for ion transport during cycling. Further research needs to be done for electrode materials of SIBs in order to determine the right structures and configuration for an optimized cell. Another key element to optimize the SIB is electrolyte investigation and selection. The effect of an electrolyte and additives on SEI layer formation and ion transport can be detrimental if not chosen correctly for specific anodic and cathodic materials. Electrolytes that are stable and do not continually decompose with cycling are preferred, and the use of additives with low salt concentration can offer these properties. Ionic liquid based electrolytes are beginning to be researched and are promising for higher voltage SIBs for transition metal redox at higher potentials, but it is still a new concept and needs continued research for effective utilization in SIBs. Overall, the outlook for the use of SIBs in current technology is favorable as long as cost, safety, cyclic stability, and energy density guidelines are met.

REFERENCES:

1 J. Liu, J. G. Zhang, Z. Yang, J. P. Lemmon, C. Imhoff, G. L. Graff, L. Li, J. Hu, C. Wang, J. Xiao, G. Xia, V. V. Viswanathan, S. Baskaran, V. Sprenkle, X. Li, Y. Shao and B. Schwenzer, *Adv. Funct. Mater.*, 2013, **23**, 929.

2 M. D. Slater, D. Kim, E. Lee and C. S. Johnson, *Adv. Funct. Mater.*, 2013, **23**, 947.

3 V. Palomares, P. Serras, I. Villaluenga, K. B. Hueso, J. Carretero-González and T. Rojo, *Energy Environ. Sci.*, 2012, **5**, 5884.

4 H. Pan, Y. S. Hu and L. Chen, *Energy Environ. Sci.*, 2013, **6**, 2338.

5 Research Center for Energy Economics http://www.ffe.de/en/the-topics/resources-and-climate-protection/6-range-assessment-of-current-lithium-reserves, Accessed: June, 2013.

6 N. Yabuuchi, K. Kubota, M. Dahbi and S. Komaba, *Chem. Rev.*, 2014, **114**, 11636.

7 S. W. Kim, D. H. Seo, X. Ma, G. Ceder and K. Kang, *Adv. Energy Mater.*, 2012, **2**, 710.

8 Elemental Abundances http://commons.wikimedia.org/wiki/File:Elemental_abundances.svg Accessed: January, 2013.

9 B. L. Ellis and L. F. Nazar, *Curr. Opin. Solid State Mater. Sci.*, 2012, **16**, 168.

10 V. Palomares, M. Casas-Cabanas, E. Castillo-Martínez, M. H. Han and T. Rojo, *Energy Environ. Sci.*, 2013, **6**, 2312.

11 M. H. Han, E. Gonzalo, G. Singh and T. Rojo, *Energy Environ. Sci.*, 2015, **8,** 81.

12 K. Mizushima, P. C. Jones, P. J. Wiseman and J. B. Goodenough, *Mater. Res. Bull.*, 1980, **15**, 783.

13 A. S. Nagelberg and W. L. Worrell, *J. Solid State Chem.*, 1979, **29**, 345.

14 J. P. Parant, R. Olazcuaga, M. Devalette, C. Fouassier and P. Hagenmuller, *J. Solid State Chem.*, 1971, **3**, 1.

15 C. Delmas, C. Fouassier and P. Hagenmuller, *Phys. B+C*, 1980, **99**, 81.

16 C. Delmas, J. Braconnier, C. Fouassier and P. Hagenmuller, *Solid State Ionics*, 1981, **3-4**, 165.

17 J. J. Braconnier, C. Delmas and P. Hagenmuller, *Mater. Res. Bull.*, 1982, **17**, 993.

18 J. J. Braconnier, C. Delmas, C. Fouassier and P. Hagenmuller, *Mater. Res. Bull.*, 1980, **15**, 1797.

19 M. S. Whittingham, *Science*, 1976, **192**, 1126.

20 M. S. Whittingham, *J. Chem. Phys.*, 1971, **54**, 414.

21 M. S. Whittingham, *J. Chem. Soc. Chem. Commun.*, 1974, 328.

22 S. P. Ong, V. L. Chevrier, G. Hautier, A. Jain, C. Moore, S. Kim, X. Ma and G. Ceder, *Energy Environ. Sci.*, 2011, **4**, 3680.

23 S. Komaba, T. Ishikawa, N. Yabuuchi, W. Murata, A. Ito and Y. Ohsawa, *ACS Appl. Mater. Interfaces*, 2011, **3**, 4165.

24 J. F. Whitacre, T. Wiley, S. Shanbhag, Y. Wenzhuo, A. Mohamed, S. E. Chun, E. Weber, D. Blackwood, E. Lynch-Bell, J. Gulakowski, C. Smith and D. Humphreys, *J. Power Sources*, 2012, **213**, 255.

25 H. Qin, Z. P. Song, H. Zhan and Y. H. Zhou, *J. Power Sources*, 2014, **249**, 367.

26 C. D. Wessells, S. V. Peddada, R. A. Huggins and Y. Cui, *Nano Lett.*, 2011, **11**, 5421.

27 C. Deng, S. Zhang, Z. Dong and Y. Shang, *Nano Energy*, 2014, **4**, 49.

28 J. F. Whitacre, a. Tevar and S. Sharma, *Electrochem. Commun.*, 2010, **12**, 463.

29 Y. Cao, L. Xiao, W. Wang, D. Choi, Z. Nie, J. Yu, L. V Saraf, Z. Yang and J. Liu, *Adv. Mater.*, 2011, **23**, 3155.

30 W. Song, X. Ji, Y. Zhu, H. Zhu, F. Li, J. Chen, F. Lu, Y. Yao and C. E. Banks, *ChemElectroChem*, 2014, **1**, 871.

31 D. J. Kim, R. Ponraj, A. G. Kannan, H. Lee, R. Fathi, R. Ruffo, C. M. Mari and D. Kyung, *J. Power Sources*, 2013, **244**, 758.

32 Y. Liu, Y. Qiao, W. Zhang, H. Xu, Z. Li, Y. Shen, L. Yuan, X. Hu, X. Dai and Y. Huang, *Nano Energy*, 2014, **5**, 97.

33 Z. Li, D. Young, K. Xiang, W. C. Carter and Y.-M. Chiang, *Adv. Energy Mater.*, 2013, **3**, 290.

34 K. Kubota, N. Yabuuchi, H. Yoshida, M. Dahbi and S. Komaba, *MRS Bull.*, 2014, **39**, 416.

35 H. Kim, D. J. Kim, D. Seo, M. S. Yeom, K. Kang, D. K. Kim and Y. Jung, *Chem. Mater.*, 2012, **24**, 1205.

36 X. Ma, H. Chen and G. Ceder, *J. Electrochem. Soc.*, 2011, **158**, A1307.

37 I. H. Jo, H. S. Ryu, D. G. Gu, J. S. Park, I. S. Ahn, H. J. Ahn, T. H. Nam and K. W. Kim, *Mater. Res. Bull.*, 2014, **3**, 2.

38 N. Yabuuchi, K. Yoshii, S. Myung, I. Nakai and S. Komaba, *J. Am. Chem. Soc.*, 2011, **133**, 4404.

39 S. Yang, X. Wang, Y. Wang, Q. Chen, J. Li and X. Yang, *Trans. Nonferrous Met. Soc. China*, 2010, **20**, 1892.

40 A. Mendiboure, C. Delmas and P. Hagenmuller, *J. Solid State Chem.*, 1985, **57**, 323.

41 J. Zhao, H. Chen, J. Shi, J. Gu, X. Dong, J. Gao, M. Ruan and L. Yu, *Microporous Mesoporous Mater.*, 2008, **116**, 432.

42 J. P. Parant, R. Olazcuaga, M. Devalette, C. Fouassier and P. Hagenmuller, *J. Solid State Chem.*, 1971, **3**, 1.

43 O. A. Vargas, A. Caballero, L. Hernán and J. Morales, *J. Power Sources*, 2011, **196**, 3350.

44 N. Bucher, S. Hartung, A. Nagasubramanian, Y. L. Cheah, H. E. Hoster and S. Madhavi, *ACS Appl. Mater. Interfaces*, 2014, **6**, 8059.

45 A. Caballero, L. Hernán, J. Morales, L. Sánchez and J. Santos, *J. Solid State Chem.*, 2003, **174**, 365.

46 F. Sauvage, L. Laffont, J. M. Tarascon and E. Baudrin, *Inorg. Chem.*, 2007, **46**, 3289.

47 J. Billaud, R. J. Clement, A. R. Armstrong, J. Canales-Vazquez, P. Rozier, C. P. Grey and P. G. Bruce, *J. Am. Chem. Soc.*, 2014, **136,** 17243.

48 S. Komaba, C. Takei, T. Nakayama, A. Ogata and N. Yabuuchi, *Electrochem. Commun.*, 2010, **12**, 355.

49 C. Y. Chen, K. Matsumoto, T. Nohira, R. Hagiwara, A. Fukunaga, S. Sakai, K. Nitta and S. Inazawa, *J. Power Sources*, 2013, **237**, 52.

50 J. J. Ding, Y.-N. Zhou, Q. Sun and Z.-W. Fu, *Electrochem. Commun.*, 2012, **22**, 85.

51 X. Xia and J. R. Dahn, *Electrochem. Solid-State Lett.*, 2012, **15**, A1.

52 S. Komaba, T. Nakayama, A. Ogata, T. Shimizu, C. Takei, S. Takada, A. Hokura and I. Nakai, *ECS Transactions*, 2009, **16,** 43.

53 Y. Takeda, K. Nakahara, M. Nishijima, N. Imanishi, O. Yamamoto, M. Takano and R. Kanno, *Mater. Res. Bull.*, 1994, **29**, 659.

54 M. Tabuchi, *Solid State Ionics*, 1996, **90**, 129.

55 M. C. Blesa, E. Moran, C. León, J. Santamaria, J. D. Tornero and N. Menéndez, *Solid State Ionics*, 1999, **126**, 81.

56 J. Zhao, L. Zhao, N. Dimov, S. Okada and T. Nishida, *J. Electrochem. Soc.*, 2013, **160**, A3077.

57 H. Yoshida, N. Yabuuchi and S. Komaba, in *ECS Meet. Abstr. MA2012-02*, 2011, vol. 201, p. 1850.

58 E. Monyoncho and R. Bissessur, *Mater. Res. Bull.*, 2013, **48**, 2678.

59 B. Koo, S. Chattopadhyay, T. Shibata, V. B. Prakapenka, C. S. Johnson, T. Rajh and E. V. Shevchenko, *Chem. Mater.*, 2013, **25**, 245.

60 N. Yabuuchi, M. Kajiyama, J. Iwatate, H. Nishikawa, S. Hitomi, R. Okuyama, R. Usui, Y. Yamada and S. Komaba, *Nat. Mater.*, 2012, **11**, 512.

61 D. Buchholz, A. Moretti, R. Kloepsch, S. Nowak, V. Siozios, M. Winter and S. Passerini, *Chem. Mater.*, 2013, **25**, 142.

62 S. M. Oh, S. T. Myung, C. S. Yoon, J. Lu, J. Hassoun, B. Scrosati, K. Amine and Y. K. Sun, *Nano Lett.*, 2014, **14**, 1620.

63 S. Doubaji, M. Valvo, I. Saadoune, M. Dahbi and K. Edström, *J. Power Sources*, 2014, **266**, 275.

64 J. Xu, S. L. Chou, J. L. Wang, H. K. Liu and S. X. Dou, *ChemElectroChem*, 2014, **1**, 371.

65 L. G. Chagas, D. Buchholz, L. Wu, B. Vortmann and S. Passerini, *J. Power Sources*, 2014, **247**, 377.

66 H. Yu, S. Guo, Y. Zhu, M. Ishida and H. Zhou, *Chem. Commun.*, 2014, **50**, 457.

67 D. Yuan, X. Hu, J. Qian, F. Pei, F. Wu, R. Mao, X. Ai, H. Yang and Y. Cao, *Electrochim. Acta*, 2014, **116**, 300.

68 J. S. Thorne, R. a. Dunlap and M. N. Obrovac, *J. Electrochem. Soc.*, 2012, **160**, A361.

69 B. Mortemard de Boisse, D. Carlier, M. Guignard and C. Delmas, *J. Electrochem. Soc.*, 2013, **160**, A569.

70 N. Yabuuchi and S. Komaba, *Sci. Technol. Adv. Mater.*, 2014, **15**, 043501.

71 J. Zhao, J. Xu, D. H. Lee, N. Dimov, Y. S. Meng and S. Okada, *J. Power Sources*, 2014, **264**, 235.

72 J. Billaud, G. Singh, A. R. Armstrong, E. Gonzalo, V. Roddatis, M. Armand, T. Rojo and P. G. Bruce, *Energy Environ. Sci.*, 2014, **7**, 1387.

73 J. Wang, J. Yang, Y. Nuli and R. Holze, *Electrochem. Commun.*, 2007, **9**, 31.

74 T. H. Hwang, D. S. Jung, J. S. Kim, B. G. Kim and J. W. Choi, *Nano Lett.*, 2013, **13**, 4532.

75 J. S. Kim, D. Y. Kim, G. B. Cho, T. H. Nam, K. W. Kim, H. S. Ryu, J. H. Ahn and H. J. Ahn, *J. Power Sources*, 2009, **189**, 864.

76 T. B. Kim, W. H. Jung, H. S. Ryu, K. W. Kim, J. H. Ahn, K. K. Cho, G. B. Cho, T. H. Nam, I. S. Ahn and H. J. Ahn, *J. Alloys Compd.*, 2008, **449**, 304.

77 J. S. Kim, G. B. Cho, K. W. Kim, J. H. Ahn, G. Wang and H. J. Ahn, *Curr. Appl. Phys.*, 2011, **11**, S215.

78 J. S. Kim, H. J. Ahn, H. S. Ryu, D. J. Kim, G. B. Cho, K. W. Kim, T. H. Nam and J. H. Ahn, *J. Power Sources*, 2008, **178**, 852.

79 P. Barpanda, J. N. Chotard, N. Recham, C. Delacourt, M. Ati, L. Dupont, M. Armand and J. M. Tarascon, *Inorg. Chem.*, 2010, **49**, 7401.

80 P. Barpanda, G. Oyama, S. I. Nishimura, S. C. Chung and A. Yamada, *Nat. Commun.*, 2014, **5**, 1.

81 K. Saravanan, C. W. Mason, A. Rudola, K. H. Wong and P. Balaya, *Adv. Energy Mater.*, 2013, **3**, 444.

82 C. Zhu, K. Song, P. A. Van Aken, J. Maier and Y. Yu, *Nano Lett.*, 2014, **14**, 2175.

83 L. S. Plashnitsa, E. Kobayashi, Y. Noguchi, S. Okada and J. Yamaki, *J. Electrochem. Soc.*, 2010, **157**, A536.

84 Y. Uebou, T. Kiyabu, S. Okada and J. ichi Yamaki, *reports Inst. Adv. Mater. Study Kyushu Univ.*, 2002, **16**, 1.

85 S. Y. Lim, H. Kim, R. A. Shakoor, Y. Jung and J. W. Choi, *J. Electrochem. Soc.*, 2012, **159**, A1393.

86 Z. Jian, L. Zhao, H. Pan, Y. S. Hu, H. Li, W. Chen and L. Chen, *Electrochem. Commun.*, 2012, **14**, 86.

87 Z. Jian, W. Han, X. Lu, H. Yang, Y. S. Hu, J. Zhou, Z. Zhou, J. Li, W. Chen, D. Chen and L. Chen, *Adv. Energy Mater.*, 2013, **3**, 156.

88 Y. H. Jung, C. H. Lim and D. K. Kim, *J. Mater. Chem. A*, 2013, **1**, 11350.

89 Q. Sun, Q. Q. Ren and Z. W. Fu, *Electrochem. Commun.*, 2012, **23**, 145.

90 J. Kang, S. Baek, V. Mathew, J. Gim, J. Song, H. Park, E. Chae, A. K. Rai and J. Kim, *J. Mater. Chem.*, 2012, **22**, 20857.

91 Y. Kawabe, N. Yabuuchi, M. Kajiyama, N. Fukuhara, T. Inamasu, R. Okuyama, I. Nakai and S. Komaba, *Electrochem. Commun.*, 2011, **13**, 1225.

92 Y. Lu, S. Zhang, Y. Li, L. Xue, G. Xu and X. Zhang, *J. Power Sources*, 2014, **247**, 770.

93 C. Vidal-Abarca, P. Lavela, J. L. Tirado, a. V. Chadwick, M. Alfredsson and E. Kelder, *J. Power Sources*, 2012, **197**, 314.

94 Y. U. Park, D. H. Seo, H. S. Kwon, B. Kim, J. Kim, H. Kim, I. Kim, H. I. Yoo and K. Kang, *J. Am. Chem. Soc.*, 2013, **135**, 13870.

95 R. K. B. Gover, A. Bryan, P. Burns and J. Barker, *Solid State Ionics*, 2006, **177**, 1495.

96 J. Barker, M. Y. Saidi and J. L. Swoyer, *Electrochem. Solid-State Lett.*, 2003, **6**, A1.

97 N. Recham, J. N. Chotard, L. Dupont, K. Djellab, M. Armand and J. M. Tarascon, *J. Electrochem. Soc.*, 2009, **156**, A993.

98 H. Zhuo, X. Wang, A. Tang, Z. Liu, S. Gamboa and P. J. Sebastian, *J. Power Sources*, 2006, **160**, 698.

99 P. Serras, V. Palomares, P. Kubiak, L. Lezama and T. Rojo, *Electrochem. Commun.*, 2013, **34**, 344.

100 M. Xu, P. Xiao, S. Stauffer, J. Song, G. Henkelman and J. B. Goodenough, *Chem. Mater.*, 2014, **26**, 3089.

101 N. Sharma, P. Serras, V. Palomares, H. E. A. Brand, J. Alonso, P. Kubiak, M. L. Fdez-Gubieda and T. Rojo, *Chem. Mater.*, 2014, **26**, 3391.

102 G. Hautier, A. Jain, H. Chen, C. Moore, S. P. Ong and G. Ceder, *J. Mater. Chem.*, 2011, **21**, 17147.

103 H. Chen, G. Hautier, A. Jain, C. Moore, B. Kang, R. Doe, L. Wu, Y. Zhu, Y. Tang and G. Ceder, *Chem. Mater.*, 2012, **24**, 2009.

104 H. Chen, G. Hautier and G. Ceder, *J. Am. Chem. Soc.*, 2012, **134**, 19619.

105 H. Chen, Q. Hao, O. Zivkovic, G. Hautier, L. Du, Y. Tang, Y. Hu, X. Ma, C. P. Grey and G. Ceder, *Chem. Mater.*, 2013, **25**, 2777.

106 C. Wang, M. Sawicki, S. Emani, C. Liu and L. Shaw, *Electrochim. Acta*, 2015, **161,** 322.

107 M. Nose, H. Nakayama, K. Nobuhara, H. Yamaguchi, S. Nakanishi and H. Iba, *J. Power Sources*, 2013, **234**, 175.

108 S. Y. Lim, H. Kim, J. Chung, J. H. Lee, B. G. Kim, J. J. Choi, K. Y. Chung, W. Cho, S. J. Kim, W. A. Goddard, Y. Jung and J. W. Choi, *Proc. Natl. Acad. Sci. U. S. A.*, 2014, **111**, 599.

109 I. D. Gocheva, M. Nishijima, T. Doi, S. Okada, J. Yamaki and T. Nishida, *J. Power Sources*, 2009, **187**, 247.

110 N. Dimov, A. Nishimura, K. Chihara, A. Kitajou, I. D. Gocheva and S. Okada, *Electrochim. Acta*, 2013, **110**, 214.

111 Y. Yamada, T. Doi, I. Tanaka, S. Okada and J. Yamaki, *J. Power Sources*, 2011, **196**, 4837.

112 A. Kitajou, H. Komatsu, K. Chihara, I. D. Gocheva, S. Okada and J. Yamaki, *J. Power Sources*, 2012, **198**, 389.

113 A. Eftekhari, *J. Power Sources*, 2004, **126**, 221.

114 L. Wang, Y. Lu, J. Liu, M. Xu, J. Cheng, D. Zhang and J. B. Goodenough, *Angew. Chem. Int. Ed.*, 2013, **52**, 1964.

115 C. D. Wessells, S. V. Peddada, M. T. McDowell, R. A. Huggins and Y. Cui, *J. Electrochem. Soc.*, 2012, **159**, A98.

116 C. D. Wessells, R. A. Huggins and Y. Cui, *Nat. Commun.*, 2011, **2**, 550.

117 Y. Lu, L. Wang, J. Cheng and J. B. Goodenough, *Chem. Commun.*, 2012, **48**, 6544.

118 Y. Yue, A. J. Binder, B. Guo, Z. Zhang, Z. A. Qiao, C. Tian and S. Dai, *Angew. Chemie*, 2014, **126**, 3198.

119 R. Alcántara, J. M. Jiménez Mateos and J. L. Tirado, *J. Electrochem. Soc.*, 2002, **149**, A201.

120 M. M. Doeff, Y. Ma, S. J. Visco and L. C. De Jonghe, *J. Electrochem. Soc.*, 1993, **140**, 169.

121 E. Zhecheva, R. Stoyanova, J. M. Jimenez-Mateos, R. Alcántara, P. Lavela and J. L. Tirado, *Carbon*, 2002, **40**, 2301.

122 R. Alcántara, P. Lavela, G. F. Ortiz and J. L. Tirado, *Electrochem. Solid-State Lett.*, 2005, **8**, A222.

123 R. Alcántara, J. M. Jimenez-Mateos, P. Lavela and J. L. T. Tirado, *Electrochem. Commun.*, 2001, **3**, 639.

124 P. Thomas, J. Ghanbaja, D. Billaud, H. Poincare and I. Nancy, *Electrochim. Acta*, 1999, **45**, 423.

125 Z. Wang, L. Qie, L. Yuan, W. Zhang, X. Hu and Y. Huang, *Carbon*, 2013, **55**, 328.

126 L. Fu, K. Tang, K. Song, P. a van Aken, Y. Yu and J. Maier, *Nanoscale*, 2014, **6**, 1384.

127 D. A. Stevens and J. R. Dahn, *J. Electrochem. Soc.*, 2001, **148**, A803.

128 S. Komaba, W. Murata, T. Ishikawa, N. Yabuuchi, T. Ozeki, T. Nakayama, A. Ogata, K. Gotoh and K. Fujiwara, *Adv. Funct. Mater.*, 2011, **21**, 3859.

129 A. Ponrouch, A. R. Goñi and M. R. Palacín, *Electrochem. Commun.*, 2013, **27**, 85.

130 J. Zhao, L. Zhao, K. Chihara, S. Okada, J. Yamaki, S. Matsumoto, S. Kuze and K. Nakane, *J. Power Sources*, 2013, **244**, 752.

131 J. Ding, H. Wang, Z. Li, A. Kohandehghan, K. Cui, Z. Xu, B. Zahiri, X. Tan, E. M. Lotfabad, B. C. Olsen and D. Mitlin, *ACS Nano*, 2013, **7**, 11004.

132 Y. Cao, L. Xiao, M. L. Sushko, W. Wang, B. Schwenzer, J. Xiao, Z. Nie, L. V Saraf, Z. Yang and J. Liu, *Nano Lett.*, 2012, **12**, 3783.

133 Y. Liu, Y. Xu, Y. Zhu, J. N. Culver, C. a Lundgren, K. Xu and C. Wang, *ACS Nano*, 2013, **7**, 3627.

134 J. Qian, X. Wu, Y. Cao, X. Ai and H. Yang, *Angew. Chem. Int. Ed.*, 2013, **52**, 4633.

135 K. Dai, H. Zhao, Z. Wang, X. Song, V. Battaglia and G. Liu, *J. Power Sources*, 2014, **263**, 276.

136 Y. Zhu, X. Han, Y. Xu, Y. Liu, S. Zheng, K. Xu, L. Hu and C. Wang, *ACS Nano*, 2013, **7**, 6378.

137 H. Zhu, Z. Jia, Y. Chen, N. Weadock, J. Wan, O. Vaaland, X. Han, T. Li and L. Hu, *Nano Lett.*, 2013, **13**, 3093.

138 M. Mortazavi, J. Deng, V. B. Shenoy and N. V. Medhekar, *J. Power Sources*, 2013, **225**, 207.

139 H. Xiong, M. D. Slater, M. Balasubramanian, C. S. Johnson and T. Rajh, *J. Phys. Chem. Lett.*, 2011, **2**, 2560.

140 Y. Xu, E. M. Lotfabad, H. Wang, B. Farbod, Z. Xu, A. Kohandehghan and D. Mitlin, *Chem. Commun.*, 2013, **49**, 8973.

141 S. M. Oh, J. Y. Hwang, C. S. Yoon, J. Lu, K. Amine, I. Belharouak and Y. K. Sun, *ACS Appl. Mater. Interfaces*, 2014.

142 P. Senguttuvan, G. Rousse, V. Seznec, J. M. Tarascon and M. R. Palacín, *Chem. Mater.*, 2011, **23**, 4109.

143 A. Rudola, K. Saravanan, C. W. Mason and P. Balaya, *J. Mater. Chem. A*, 2013, **1**, 2653.

144 W. Wang, C. Yu, Y. Liu, J. Hou, H. Zhu and S. Jiao, *RSC Adv.*, 2013, **3**, 1041.

145 Y. Zhang, L. Guo and S. Yang, *Chem. Commun.*, 2014, **50**, 14029.

146 H. Yu, Y. Ren, D. Xiao, S. Guo, Y. Zhu, Y. Qian, L. Gu and H. Zhou, *Angew. Chem. Int. Ed.*, 2014, **53**, 8963.

147 A. Rudola, K. Saravanan, S. Devaraj, H. Gong and P. Balaya, *Chem. Commun.*, 2013, **49**, 7451.

148 S. Yuan, X. Huang, D. Ma, H. Wang, F. Meng and X. Zhang, *Adv. Mater.*, 2014, **26**, 2273.

149 J. Y. Jang, H. Kim, Y. Lee, K. T. Lee, K. Kang and N. S. Choi, *Electrochem. Commun.*, 2014, **44**, 74.

150 A. Ponrouch, E. Marchante, M. Courty, J.-M. Tarascon and M. R. Palacín, *Energy Environ. Sci.*, 2012, **5**, 8572.

151 A. Ponrouch, D. Monti, A. Boschin, B. Steen, P. Johansson and M. R. Palacín, *J. Mater. Chem. A*, 2015, **3**, 22.

152 A. Ponrouch, R. Dedryvère, D. Monti, A. E. Demet, J. M. Ateba Mba, L. Croguennec, C. Masquelier, P. Johansson and M. R. Palacín, *Energy Environ. Sci.*, 2013, **6**, 2361.

153 D. Monti, E. Jónsson, M. R. Palacín and P. Johansson, *J. Power Sources*, 2014, **245**, 630.

154 J. Serra Moreno, G. Maresca, S. Panero, B. Scrosati and G. B. Appetecchi, *Electrochem. Commun.*, 2014, **43**, 1.

155 M. Dahbi, T. Nakano, N. Yabuuchi, T. Ishikawa, K. Kubota, M. Fukunishi, S. Shibahara, J.-Y. Son, Y.-T. Cui, H. Oji and S. Komaba, *Electrochem. Commun.*, 2014, **44**, 66.

156 B. Koo, H. Kim, Y. Cho, K. T. Lee, N. S. Choi and J. Cho, *Angew. Chem. Int. Ed.*, 2012, **51**, 8762.

157 M. H. Ryou, J. Kim, I. Lee, S. Kim, Y. K. Jeong, S. Hong, J. H. Ryu, T. S. Kim, J. K. Park, H. Lee and J. W. Choi, *Adv. Mater.*, 2013, **25**, 1571.

158 K. Gotoh, T. Ishikawa, S. Shimadzu, N. Yabuuchi, S. Komaba, K. Takeda, A. Goto, K. Deguchi, S. Ohki, K. Hashi, T. Shimizu and H. Ishida, *J. Power Sources*, 2013, **225**, 137.

159 Boston Power http://www.boston-power.com/resources/glossary Accessed: November, 2014.

160 Z. Yang, J. Liu, S. Baskaran, C. H. Imhoff and J. D. Holladay, *JOM*, 2010, **62**, 14.

161 J. J. Lee, in *Peer Review and Update Meeting 2014-U.S. Department of Energy Storage Systems Program (ESSP) Peer Review*, Washington, D.C., September, 2014.

162 W. Wang, in *Peer Review and Update Meeting 2014-U.S. Department of Energy Energy Storage Systems Program (ESSP) Peer Review*, Washington, D.C., September, 2014.

163 M. Dahbi, N. Yabuuchi, K. Kubota, K. Tokiwa and S. Komaba, *Phys. Chem. Chem. Phys.*, 2014, **16**, 15007.

164 H. Wu, G. Chan, J. W. Choi, I. Ryu, Y. Yao, M. T. McDowell, S. W. Lee, A. Jackson, Y. Yang, L. Hu and Y. Cui, *Nat. Nanotech.*, 2012, **7**, 310.

165 T. Mueller, G. Hautier, A. Jain and G. Ceder, *Chem. Mater.*, 2011, **23**, 3854.

Table 1. Sodium and Lithium characteristics[2,4]

Sodium	**Lithium**	**Category**
1.06	0.76	Cation radius, Å
23 g mol^{-1}	6.9 g mol^{-1}	Atomic Weight
-2.7 V	-3.04 V	E° (vs. SHE)
97.7°C	180.5°C	Melting Point
$150/ton	$5000/ton	Cost, carbonates
At $2,000-2,500/ton	Cu $7,000-8,500/ton	Cost, current collectors at the anode
1165	3829	Capacity (mAh g^{-1}), metal
Octahedral and prismatic	Octahedral and tetrahedral	A-O Coordination Preference

Table 2. Some cathode materials with promising capacities and cycle stability

Material	Specific capacity [mAh g^{-1}]	Charge/discharge cycles demonstrated	Ref.
$Na_{0.44}MnO_2$	120	1,000	29
α-Fe_2O_3/C nanotubes	99	500	59
$Na_3V_2(PO_4)_3$/C	30	30,000	81
$Na_3V_2(PO_4)_3$/graphene	90	300	88
$Na_{1.5}VPO_{4.8}F_{0.7}$	130	500	94
$Na_{0.45}Ni_{0.22}Co_{0.11}Mn_{0.66}O_2$	135	250	61
$Na_2MnFe(CN)_6$	145	1,200	161
$K_{0.6}Ni_{1.2}Fe(CN)_6 \cdot 3.6H_2O$	52	5,000[a)]/1,000[b)]	26[c)]
$Na_xFe_yMn_{1-y}O_2$	190	30-40	60,71

[a)] Na^+ insertion [b)] K^+ insertion [c)] With an aqueous electrolyte.

Table 3. Some anode materials with promising capacities and cycle stability

Material	Specific capacity [mAh g^{-1}]	Charge/discharge cycles demonstrated	Ref.
Hard carbon	300	120	128
Carbon nanostructure	298	210	131
Sn	400	150	133
CuO nanowires	300	450	148
$Na_2Ti_3O_7$	107	500	145
$Na_{2/3}Co_{1/3}Ti_{2/3}O_2$	90	3,000	146
$Na_2Ti_6O_{13}$	40	5,000	147

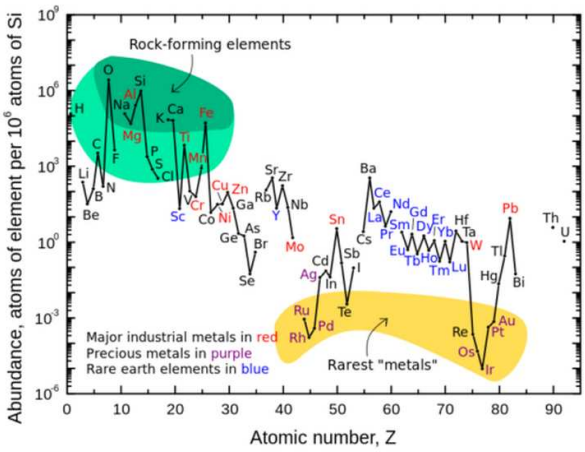

Figure 1. Abundance of elements in the earth's crust [4,7,8].

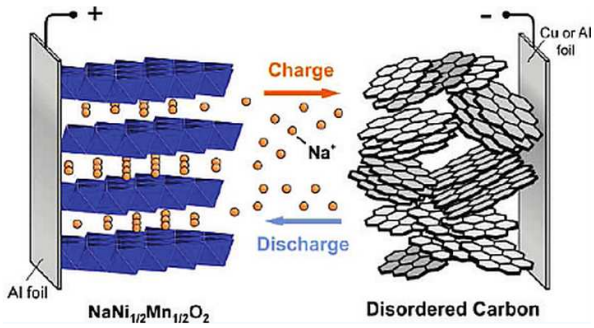

Figure 2. Schematic of sodium ion batteries with a layered transition metal oxide cathode and carbonaceous anode. Reproduced with permission [23] © 2011, ACS Publications

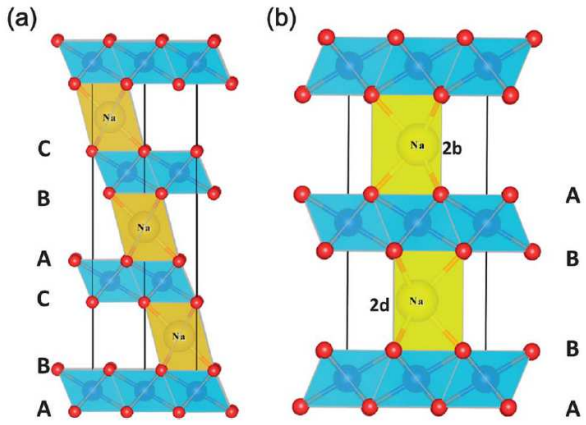

Figure 3. The crystal structure of (a) O3 and (b) P2 phases in A_xMO_2. Reproduced with permission[4] © 2013, RSC Publishing

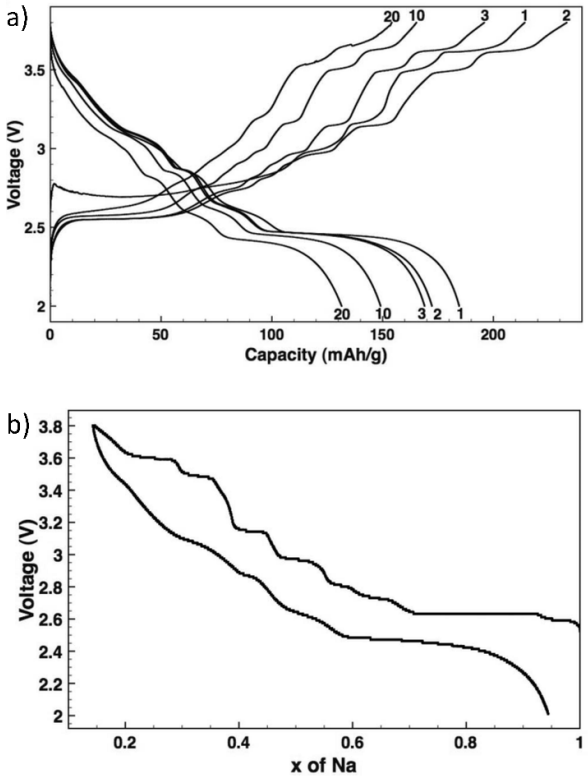

Figure 4. Voltage profiles: (a) Na_xMnO_2 cycled at C/10 with the cycle numbers indicated, and (b) Na_xMnO_2 de/sodiation as measured by potentiostatic intermittent titration. Reproduced with permission[36] © 2012, The Electrochemical Society

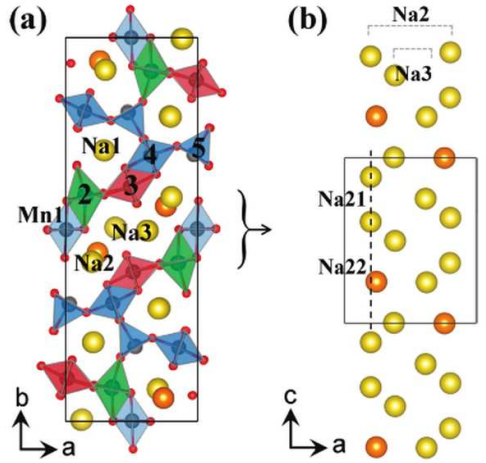

Figure 5. (a) Crystal structure of $Na_{0.44}MnO_2$ showing Mn and Na binding sites, and (b) the S shaped tunnel configuration along c-axis with different sodium positions Na21 and Na22 in $Na_{0.44}MnO_2$. Reproduced with permission[35] © 2012, ACS Publications

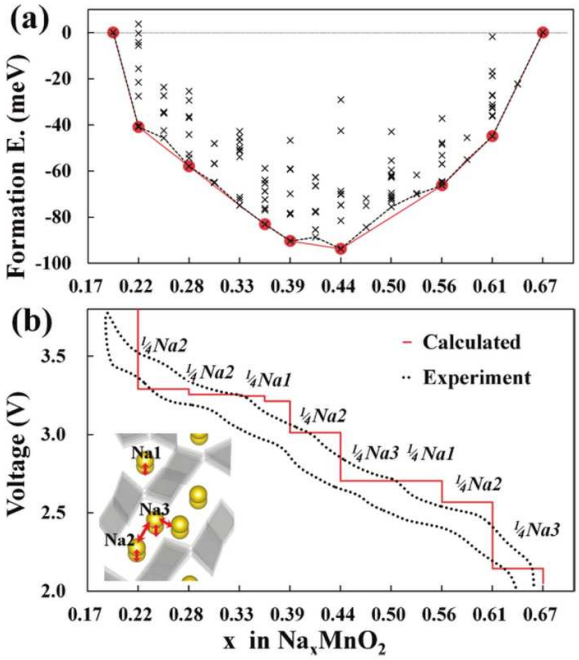

Figure 6. (a) Formation energies of seven stable intermediate phases during Na_xMnO_2 cycling calculated from 156 different sodium configurations, and (b) experimental and calculated voltage profiles for Na_xMnO_2 with respect to the minimum energy path of formation energies. Reproduced with permission[35] © 2012, ACS Publications

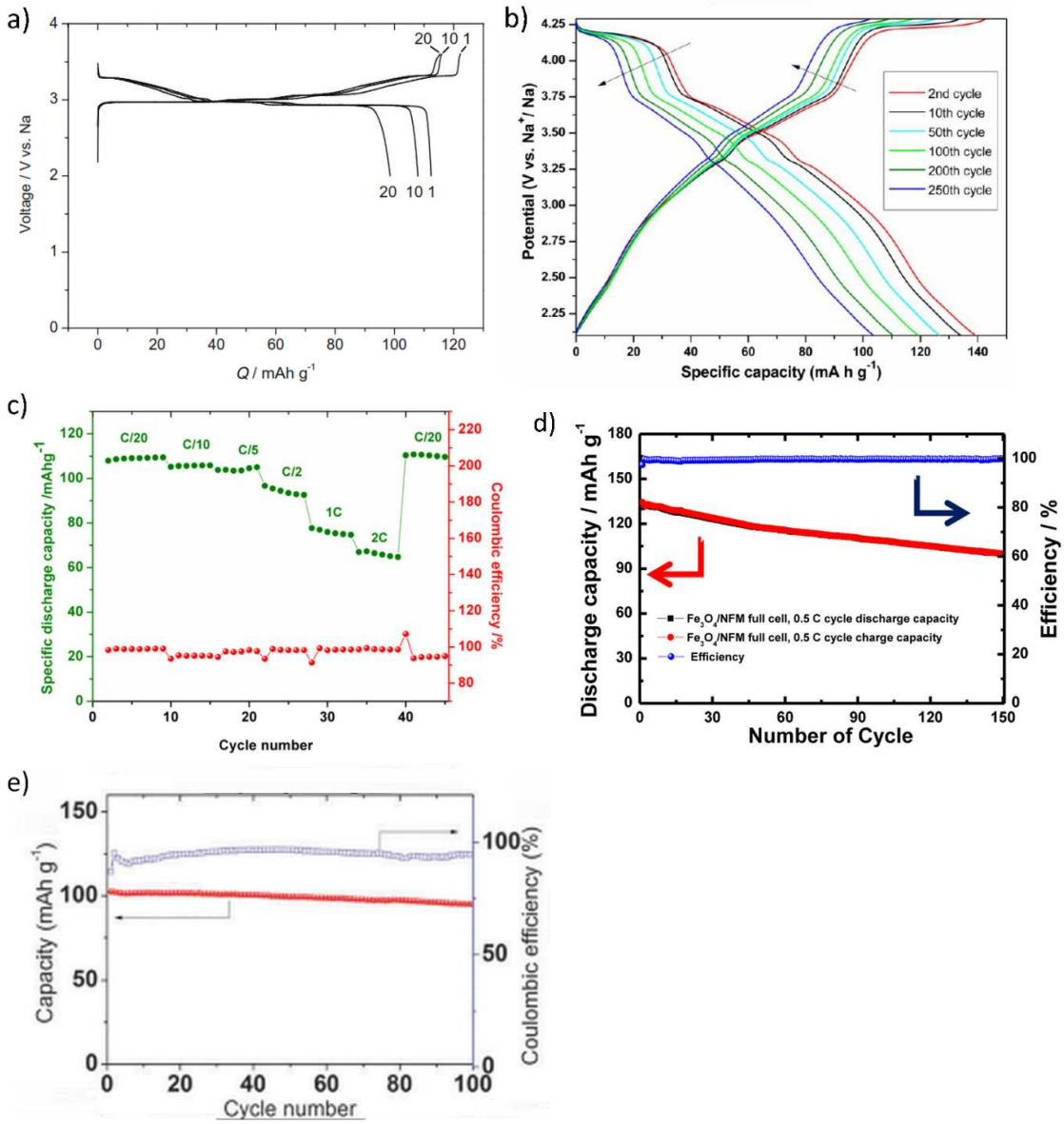

Figure 7. Charge/discharge profiles of (a) $NaCrO_2$ (Reproduced with permission[48] ©2010 Elseveir) and (b) $Na_{0.45}Ni_{0.22}Co_{0.11}Mn_{0.66}O_2$ (Reproduced with permission[61] © 2013, ACS Publications). Discharge capacities with respect to the cycle number of (c) $Na_{2/3}Co_{2/3}Mn_{2/9}Ni_{1/9}O_2$ (Reproduced with permission[63] © 2014, Elseveir), (d) $Na[Ni_{0.25}Fe_{0.5}Mn_{0.25}]O_2$ (reproduced with permission[62] © 2014, ACS Publications), and (e) $NaNi_{0.5}Ti_{0.5}O_2$ (Reproduced with permission[66] © 2014, RSC Publishing).

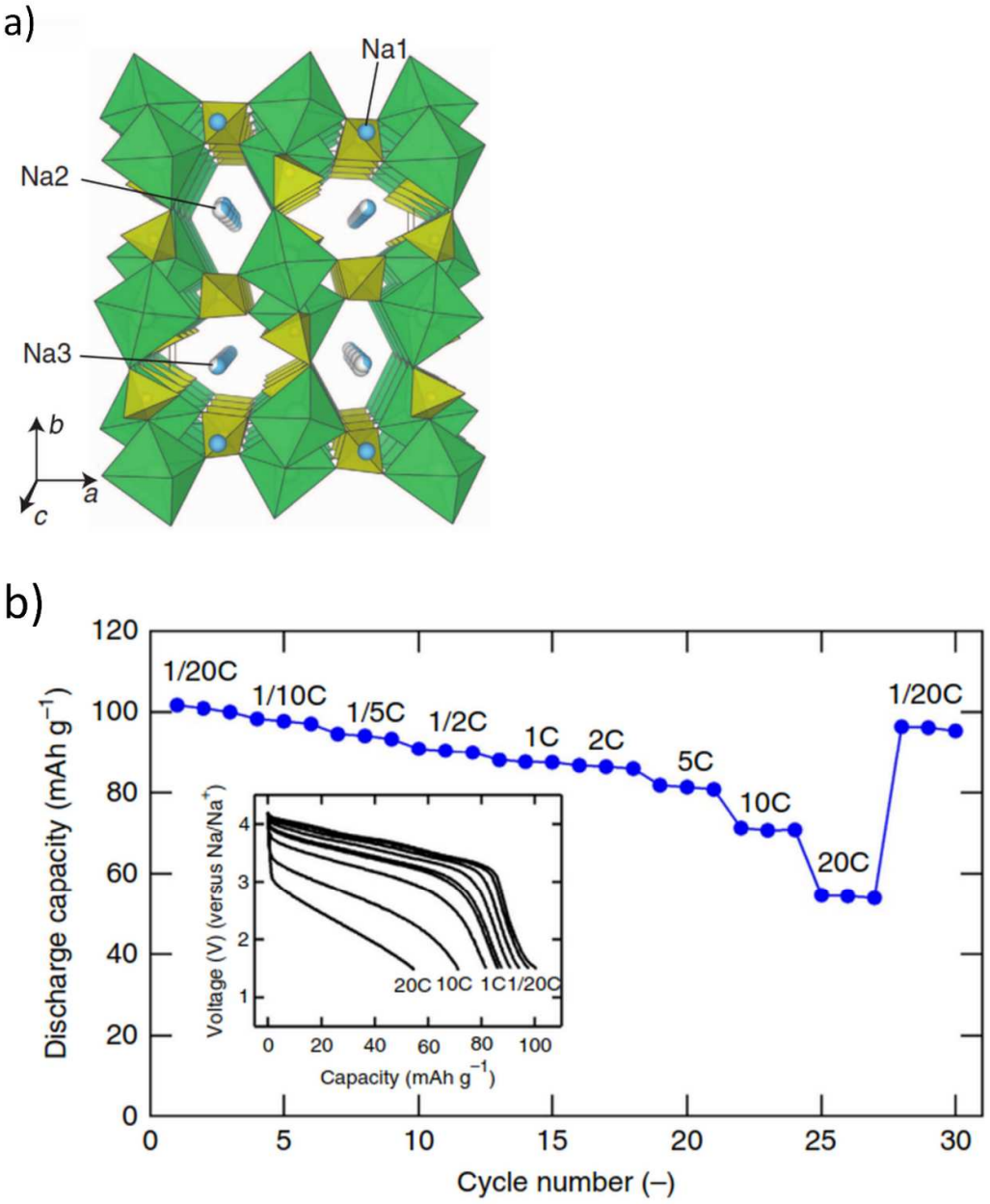

Figure 8. (a) $Na_2Fe_2(SO_4)_3$ structure projected along the c axis, and (b) capacity retention upon cycling up to 30 cycles under various rate of C/20 (2 Na in 20 h) to 20 C. Reproduced with permission[80] © 2014, Nature Publishing Group

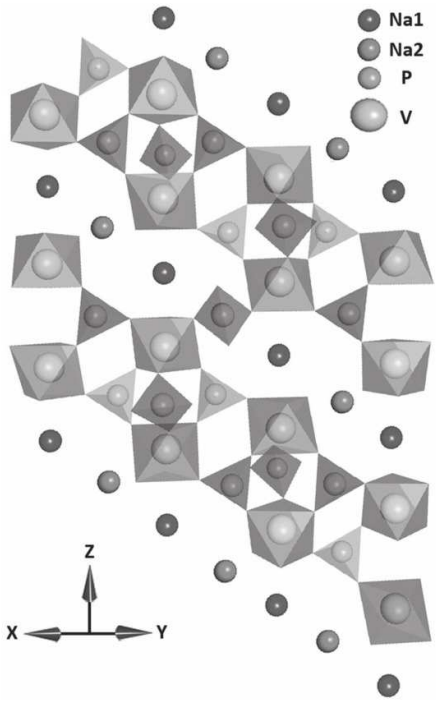

Figure 9. The crystal structure of $Na_3V_2(PO_4)_3$ in the a-b plane. Reproduced with permission[81] © 2013, WILEY-VCH Verlag GmbH & Co.

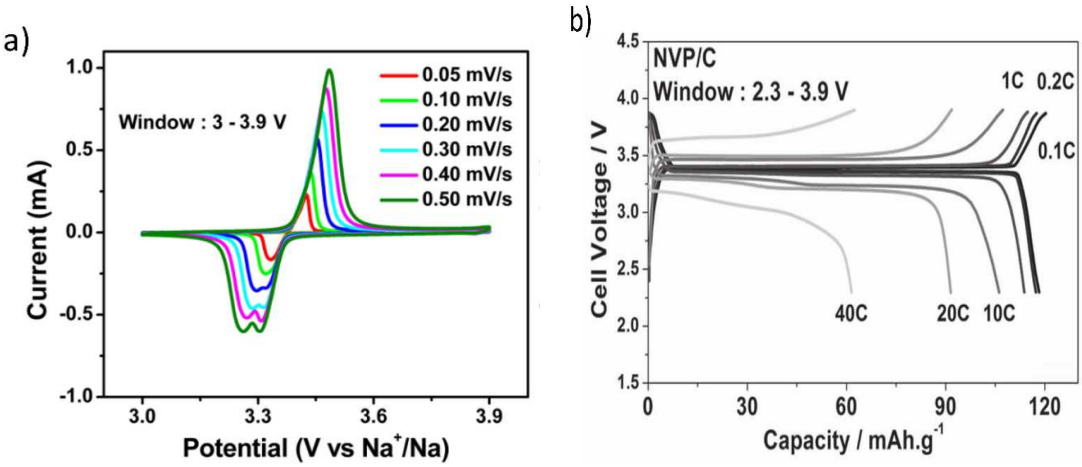

Figure 10. (a) Cyclic voltammogram of $Na_3V_2(PO_4)_3$, and (b) galvanostatic charge and discharge profiles for several C rates. Reproduced with permission[81] © 2013, WILEY-VCH Verlag GmbH & Co.

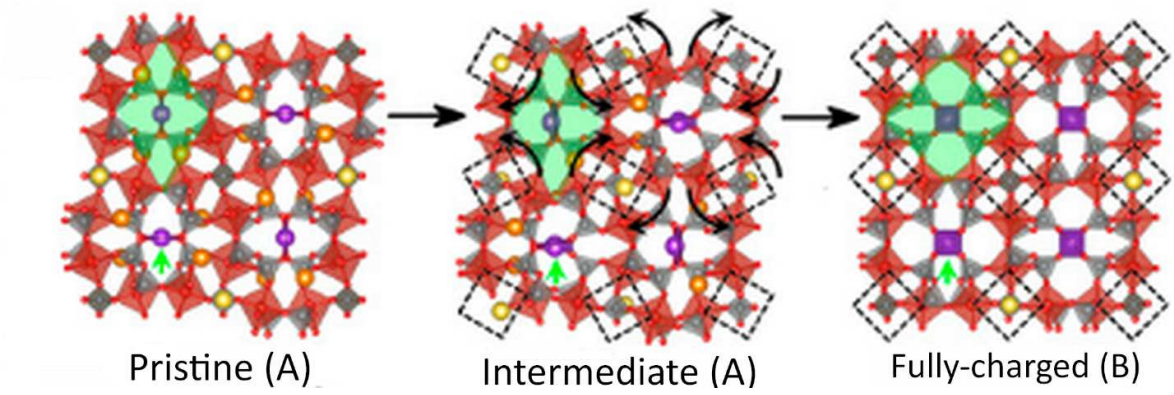

Figure 11. Structure rearrangement of VODP during phase transformation between pristine and charged phases. Crystallographically different sodium sites are colored with different colors (Na1, orange; Na2, violet; Na3, yellow). Reproduced with permission[108] © 2014, PNAS Publishing Group

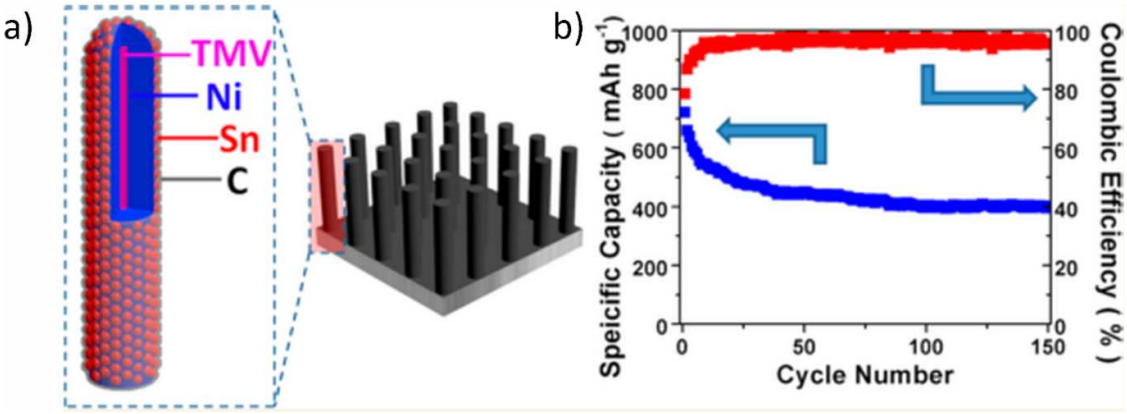

Figure 12. (a) Schematic illustration of the hierarchical structure of the 3D C/Sn/Ni/TMV1cys anode nanorod arrays, and b) cycling performance of the 3D C/Sn/Ni/TMV1cys anode. Reproduced with permission[133] © 2013, ACS Publications

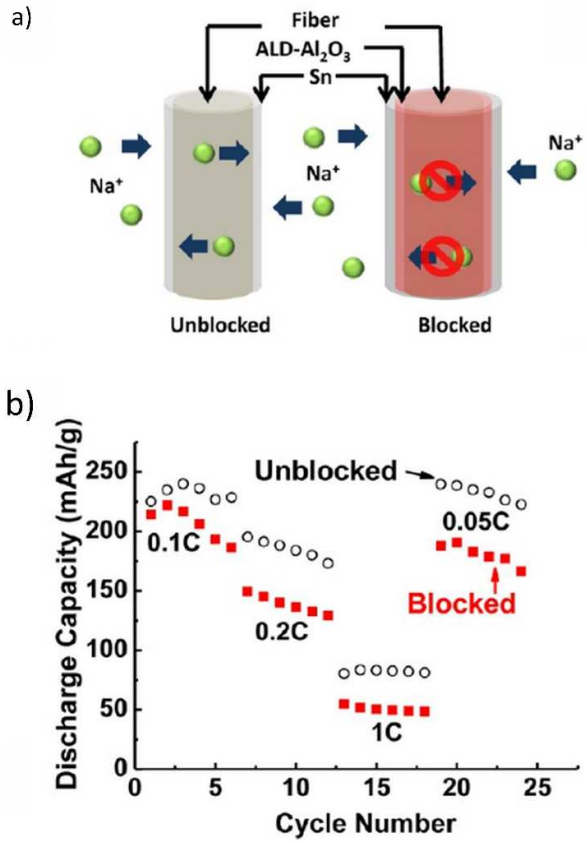

Figure 13. (a) Na ions transport along and diffuse through the mesoporous wood fiber structure. Internal transport pathways are blocked by the conformal Al_2O_3 coating, and (b) the rate performance of the Sn anode deposited on the carbon-coated mesoporous wood fibers. Reproduced with permission[137] © 2013, ACS Publications

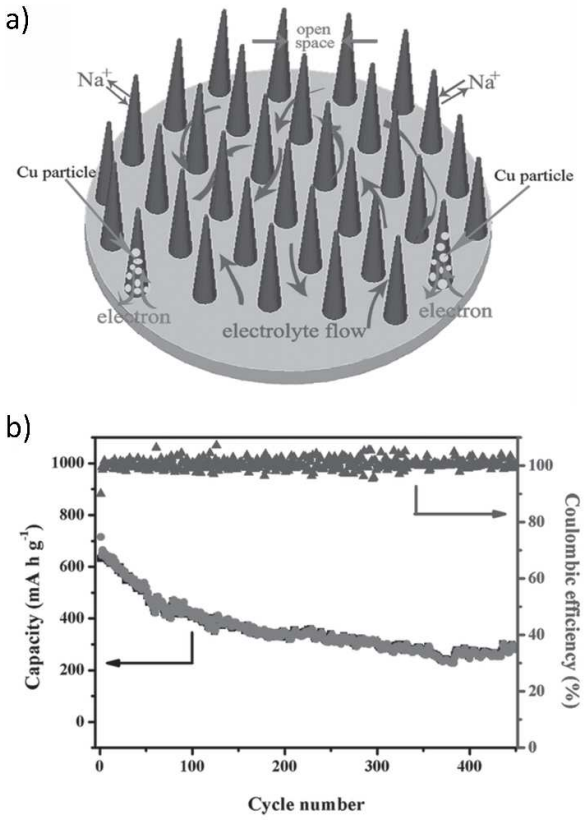

Figure 14. (a) Binder free CuO nanowire array (CNA) electrode, and (b) cycling performance of the binder free CNA (current density 200 mA g^{-1}). Reproduced with permission[148] © 2014, WILEY-VCH Verlag GmbH & Co.

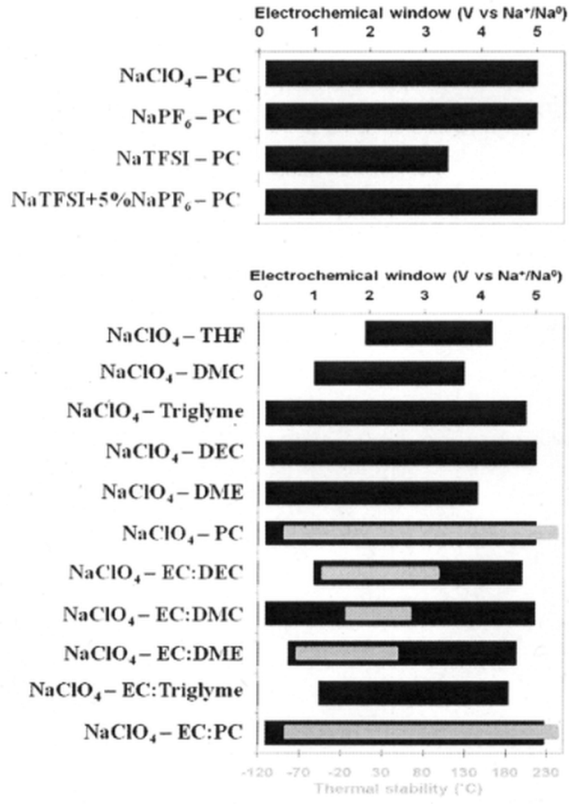

Figure 15. Electrochemical potential window stability of various salts with PC and $NaClO_4$ in various solvents. Reproduced with permission[150] © 2012, RSC Publishing

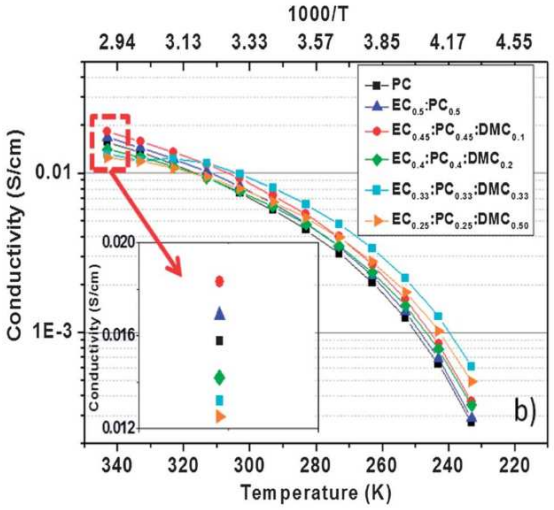

Figure 16. Arrhenius plots of the conductivity of the electrolyte based on 1 M NaTFSI salt dissolved in various solvent mixtures. Reproduced with permission[152] © 2013, RSC Publishing

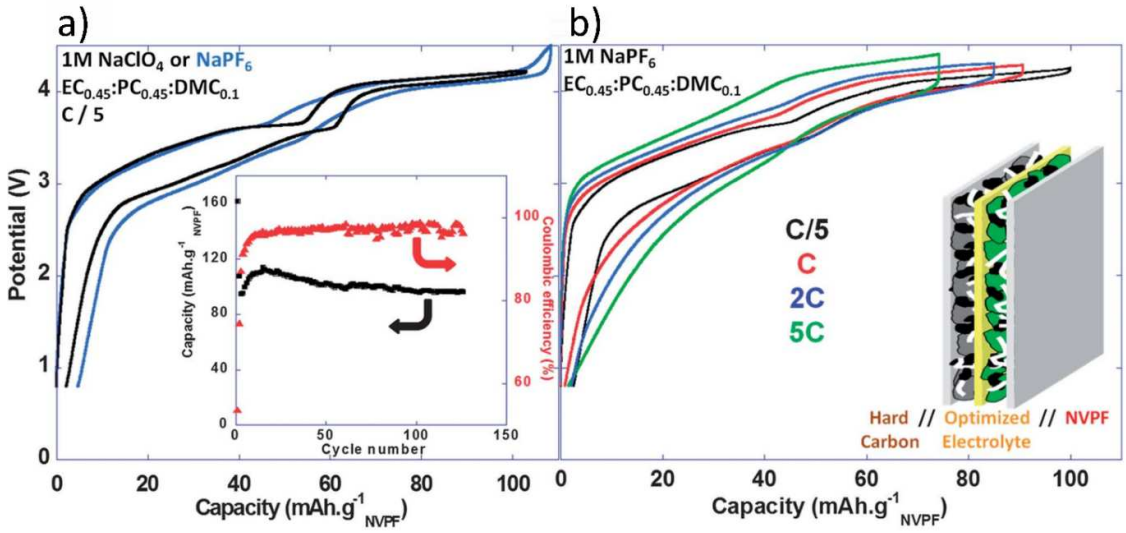

Figure 17. (a) Voltage versus capacity profiles for NVPF‖HC full Na-ion cells cycled in 1M $NaPF_6$ or 1M $NaClO_4$ in $EC_{0.45}$:$PC_{0.45}$:$DMC_{0.1}$ recorded at C/5 (inset: charge capacity and coulombic efficiency versus cycle number (C/5; 1M $NaClO_4$ in $EC_{0.45}$:$PC_{0.45}$:$DMC_{0.1}$), and (b) voltage versus capacity profiles for NVPF‖HC full Na- ion cells cycled in 1 M $NaPF_6$ in $EC_{0.45}$:$PC_{0.45}$:$DMC_{0.1}$ recorded at different rates. Reproduced with permission[152] © 2013, RSC Publishing

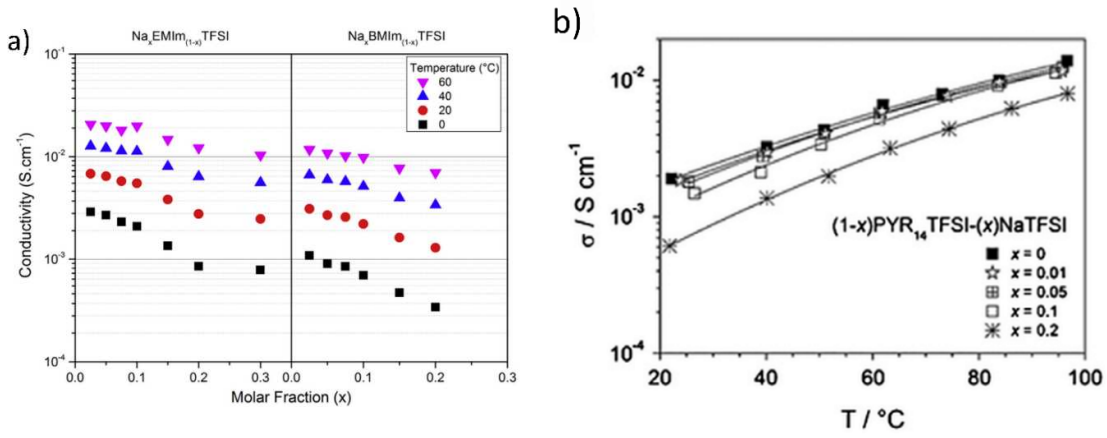

Figure 18. (a) Isotherms of the conductivity as a function of the molar fraction of Na_x-$EMIm_{(1-x)}TFSI$ and $Na_xBMIm_{(1-x)}TFSI$ (Reproduced with permission[153] © 2014, Elseveir) and (b) ionic conductivity vs. temperature for the $(1-x)PYR_{14}TFSI–(x)NaTFSI$ electrolyte. Reproduced with permission[154] © 2014, Elseveir

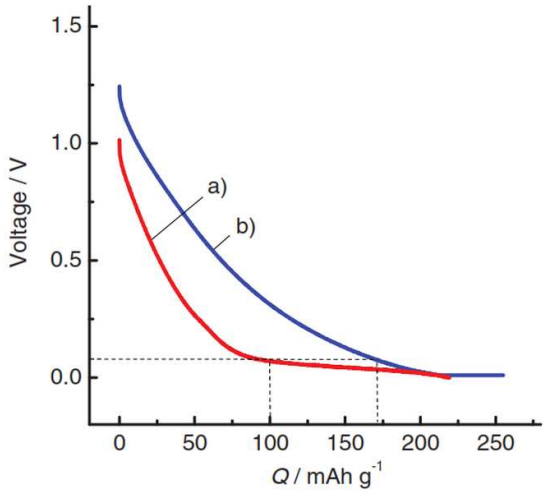

Figure 19. Chronopotentiograms of the second reduction for hard-carbon electrodes in (a) 1 mol dm^{-3} $NaClO_4$ and (b) 1 mol dm^{-3} $LiClO_4$ PC solution in Na and Li cells, respectively, at a rate of 25 mA g^{-1}. Reproduced with permission[128] © 2011, WILEY-VCH Verlag GmbH & Co.

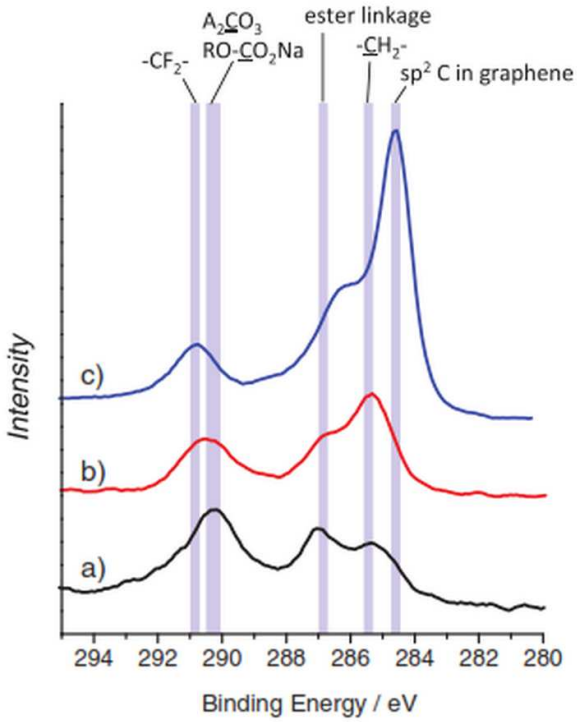

Figure 20. XPS carbon 1s spectra for the hard-carbon electrodes tested in (a) sodium and (b) lithium cells after the first cycle, and (c) pristine electrode. Reproduced with permission[128] © 2011, WILEY-VCH Verlag GmbH & Co.

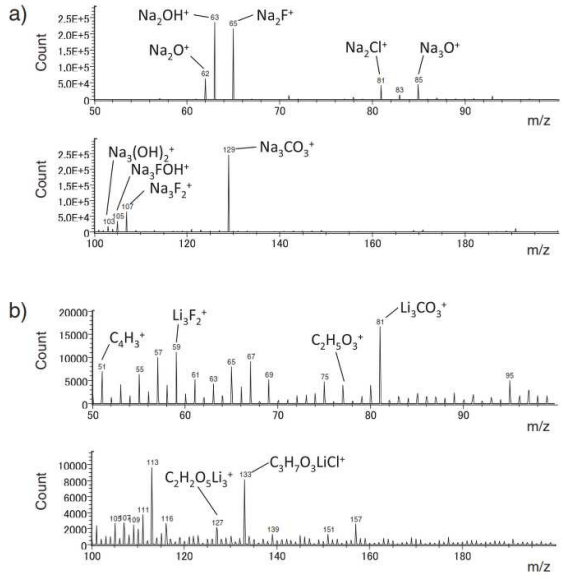

Figure 21. TOF-SIMS positive ion spectra for the hard-carbon electrodes after the first galvanostatic cycle in (a) sodium and (b) lithium cells. Reproduced with permission[128] © 2011, WILEY-VCH Verlag GmbH & Co.

A table of contents entry

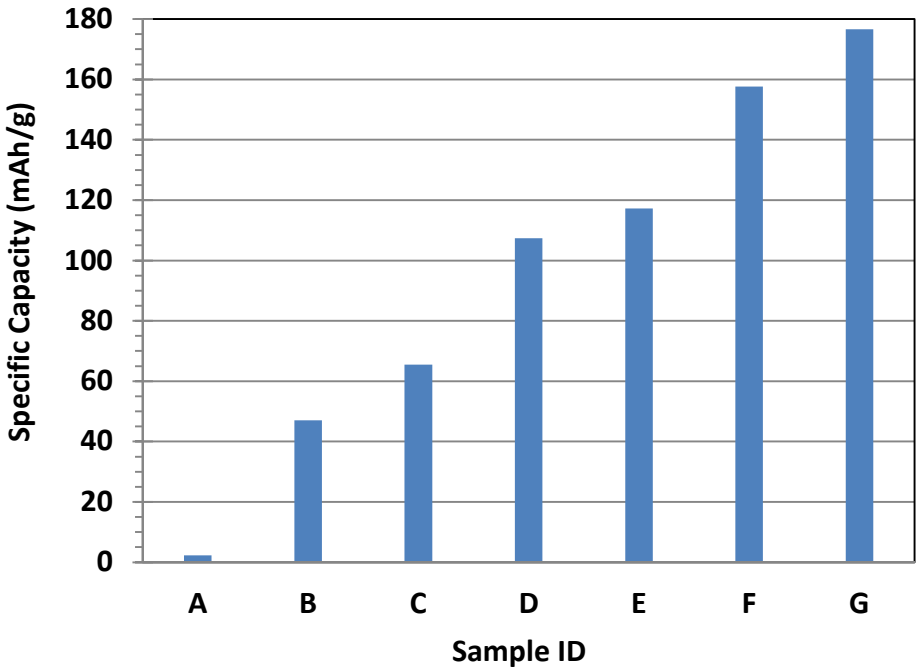

$Na_3MnCO_3PO_4$ offers a specific capacity of 176.7 mAh/g, reaching 92.5% of its theoretical if electronic conductivity is sufficient.[106]